SILICON-GERMANIUM ALLOYS FOR OPTOELECTRONIC APPLICATIONS

Xiaodong Xiao

A DISSERTATION
PRESENTED TO THE FACULTY
OF PRINCETON UNIVERSITY
IN CANDIDACY FOR THE DEGREE
OF DOCTOR OF PHILOSOPHY

RECOMMENDED FOR ACCEPTANCE
BY THE DEPARTMENT OF
ELECTRICAL ENGINEERING

June 1993

This work was supported by NSF (ECS-865-7227), ONR (N00014-90-J-1316), and NJCST

To Fei and Frank

Abstract

We have developed an all-silicon vertical-cavity Fabry-Perot optical intensity modulator operating at 1.3μm. The device utilizes free-carrier effects in silicon, with the carriers being injected into the active region of the device through a forward biased p-i-n diode. The optical cavity was formed using two $Si/SiO_2/Si$ stacks as high reflectivity mirrors. The device had a -3 dB bandwidth of 40 MHz, and a modulation depth of 10% has been achieved at a driving current density of $6 \times 10^3 A/cm^2$. The optical insertion loss of this device was less than 4 dB.

We have examined the band alignment of strained $Si_{1-x}Ge_x/Si$ heterojunctions through a comparative study of band-edge photoluminescence from strained $Si_{1-x}Ge_x$ single wells and stepped wells. Our results clearly indicate type-I band alignment for Si-rich alloys ($x \leq 0.35$) within the experimental accuracy of 5 meV. We then determined the complete band line-up for strained $Si_{1-x}Ge_x/Si$ by a combination of band-edge photoluminescence and heterojunction internal photoemission techniques.

We have studied the excitation dependent photoluminescence line-shapes in strained $Si/Si_{1-x}Ge_x/Si$ quantum wells at 77K. We have shown that luminescence is due to electron-hole plasmas, and its line-shape can be fit very well by a simple convolution of occupied electron and hole densities of states

We have experimentally observed quantum confinement shifts of band-edge photoluminescence in $Si/Si_{1-x}Ge_x/Si$ quantum wells. We have also shown that the amount of shift in PL energy can be accurately accounted for by the shift of hole ground-state energy due to size quantization

We have demonstrated for the first time $Pd_2Si/Si_{1-x}Ge_x$ and $PtSi/Si_{1-x}Ge_x$ long-wavelength infrared detectors. We have shown that by introducing a thin silicon sacrificial layer for the formation of silicide on top of $Si_{1-x}Ge_x$ reduced Schottky-barrier heights can be obtained in $PtSi/Si_{1-x}Ge_x$ ($Pd_2Si/Si_{1-x}Ge_x$) detectors, compared to those of PtSi/Si (Pd_2Si/Si) detectors. A modified Fowler theory is proposed to model the effects on the detectors' spectral response of an interfacial barrier due to unconsumed silicon sacrificial layer.

Acknowledgements

My stay at Princeton as a graduate student has been the most challenging and, at the same time, the most rewarding five years in my life. I owe a great deal of thanks to many people who have helped me throughout these years.

First of all, I would like to thank my research advisor Professor James Sturm. Nothing in this thesis would have been possible without the constant guidance, encouragement, and support he has given me in the past five-and-a-half years.

I am also in debt to all the faculty members of the Electronic Materials and Devices Group in the Department of Electrical Engineering at Princeton. Special thanks should go to Professor Sigurd Wagner and Professor Stephen Forrest, who took their time reading this thesis.

I would also like to thank my colleagues in Prof. Sturm's group, Peter M. Garone, Peter V. Schwartz, Erwin J. Prinz, Venki Venkataraman, Zeljka Matutinovic, Qun Mi, Chee-Wee Liu, and Anthony St. Amour, as well as all our fellow graduate students in the Department of Electrical Engineering at Princeton. I will never forget the friendship and partnership with them that has been built up over the years.

I am very grateful that I have had the opportunities to collaborate with Dr. S. Palfrey, Dr. D. Meyerhofer, and Dr. F. Shallcross of David Sarnoff Research Center at Princeton, Dr. R. Gregory, Dr. P. Fejes of Motorola, L.C. Lenchyshyn and Dr. M.L.W. Thewalt of Simon Fraser University.

Finally, I like to thank my parents for their understanding and support.

Contents

Chapter 1

Introduction

1.1 Motivation

In the last several decades, semiconductor technology has made tremendous progress through ever higher levels of integration largely made possible by the shrinking of feature size. Entering the Ultra-Large-Scale-Integration (ULSI) era 28 years after the invention of the transistor, we are now very close to the ultimate limit of device scaling imposed by fundamental physics Integrated optoelectronics, which combines the advantages of electronics with those of optics, offers new ways for growth. Integrating active optoelectronic devices on silicon can in many ways enhance the performance of silicon based integrated circuits (IC's). They can provide ultrafast interconnects, new functions, and possibly lower production cost.

Strained $Si_{1-x}Ge_x$ alloys have attracted an enormous amount of attention because of their potential applications in very fast electronic circuits and the possibilities of new silicon-based optoelectronic devices, such as infrared detectors and light-emitting devices. As a new material system, many of its fundamental properties, which include band alignment and luminescence properties of $Si/Si_{1-x}Ge_x/Si$ quantum wells, are yet to be understood.

This thesis treats silicon-germanium based optoelectronic devices and relevant

material properties. Research projects in this thesis include the development of an all-silicon optical intensity modulator at 1.3μm, determination of the band alignment at strained $Si_{1-x}Ge_x$/Si interfaces, photoluminescence studies of strained Si/$Si_{1-x}Ge_x$/Si quantum wells, and the development of silicide/$Si_{1-x}Ge_x$ long-wavelength infrared detectors.

1.2 Thesis outline

In Chapter 2, the development of an all-silicon optical intensity modulator at 1.3μm for fiber optics is reviewed. It starts with a brief discussion of the relevant optical properties of silicon, including free-carrier effects upon which the operation of our modulator is based. Then the device structure, fabrication, and experimental results will be presented. This chapter ends with a discussion of the ultimate performance limit of this type of device.

After a brief introduction to $Si_{1-x}Ge_x$ alloys in Chapter 3, Chapters 4 & 5 focus on some electrical and optical properties of this new material system.

In Chapter 4, a comparative study of photoluminescence from Si/$Si_{1-x}Ge_x$/Si single quantum-wells and Si/$Si_{1-y}Ge_y$/$Si_{1-x}Ge_x$/$Si_{1-y}Ge_y$/Si stepped quantum-wells is reviewed. This study provides direct evidence of type-I band alignment for strained silicon-germanium alloys on (100) silicon substrates. By combining results from internal-photoemission measurements of valence band offsets of Si/$Si_{1-x}Ge_x$ heterojunctions with bandgap energies obtained from band-edge PL, the complete band alignment of strained SiGe on silicon has been determined experimentally.

Chapter 5 covers two different photoluminescence studies of the strained silicon-germanium quantum wells : electron-hole plasmas and quantum confinement effects. First, a systematic study of the power-dependent photoluminescence line shape of a narrow quantum well and a thick $Si_{1-x}Ge_x$ film is described. A self-consistent model

which attributes the luminescence to an electron-hole plasma confined in the $Si_{1-x}Ge_x$ quantum well is proposed. Second, an experimental study of the quantum confinement shift of photoluminescence from a $Si/Si_{1-x}Ge_x/Si$ quantum well is reviewed. The results are then compared to a theoretical calculation of hole confinement energy based on a $\{6 \times 6\}$ Luttinger-Kohn effective mass Hamiltonian.

In Chapter 6 the development of silicide/$Si_{1-x}Ge_x$ long-wavelength infrared detectors is reviewed. Experimental results on Schottky-barrier height, reverse leakage current, spectral response and quantum efficiency are summarized.

The thesis ends with a chapter (Chapter 7) which summarizes the most significant contributions of this thesis and discusses possible future research directions

Chapter 2

All-silicon Optical Intensity Modulator at 1.3μm

The ability to make active optoelectronic devices in silicon which can be used as interfaces between silicon electronic circuitry and fiber optics is of great technological importance. These devices can be light emitters or modulators which transmit data by modulating an off-chip light source. Since silicon is an indirect bandgap semiconductor and does not have a linear electro-optic effect (Pockels effect) due to its inversion symmetry, making silicon electro-optic modulators is difficult. Nevertheless, there have been a few attempts at making silicon optical modulators in the wavelength range of 1.3–1.55μm [1, 2]. Hemenway et al [2] fabricated a back-illuminated reflection type intensity modulator at 1.3μm based on free-carrier effects with a 3dB bandwidth of 200 MHz. In their device, a current density of $10^5 A/cm^2$ was required to achieve a modulation depth of 10%. In this thesis, a silicon Fabry-Perot intensity modulator at 1.3μm using free-carrier effects requiring a smaller current density at comparable modulation depth and speed has been demonstrated.

2.1 Free-carrier effects

Silicon crystallizes in the diamond lattice structure. It has an indirect fundmental band-gap of 1.17eV at zero Kelvin, with the valence band maximum located at the zone-center Γ and the conduction band minima along the Δ axis 85% of the way from zone-center Γ to the X point. The indirect nature of the fundamental band-gap makes silicon an inefficient light emitter because the radiative recombination of an electron and a hole must involve participation of a momentum conserving phonon in addition to the photon, i.e., it is a weak second order process. For the same reason, the interband absorption edge of silicon near its band-gap has the onset characteristic of an indirect band-gap semiconductor:

$$\alpha \sim (h\nu - E_g)^2, \tag{2.1}$$

where α is the absorption coefficient, $h\nu$ is the photon energy, and E_g is the band-gap. In contrast, the absorption edge of a direct band-gap semiconductor has a onset shape given by (ignoring the contribution from excitons)

$$\alpha_d \sim \sqrt{h\nu - E_g}, \tag{2.2}$$

which has a much sharper turn-on at the direct band-gap. As a consequence of the slow onset near the band-gap, the Franz-Keldysh effect (change in the absorption coefficient with an applied electric field), and electrorefraction effect (change in the refractive index with an applied field) in an indirect semiconductor such as silicon are very weak and not suitable for device applications.

Another effect which has been utilized in making optical modulators is the Pockels Effect, or the linear electro-optic effect. In the most general form, the polarization vector $\mathbf{P}$ of a material under an applied electric field $\mathbf{E}$ is given by:

$$P_i = \sum_j \alpha_{ij} E_j + \sum_{j,k} \chi_{ijk} E_j E_k + \ldots \tag{2.3}$$

For some materials, such as $LiNbO_3$, and III-V compound semiconductors, the linear electro-optic effect coefficients χ_{ijk} are not all zero. As a result, the dielectric constant of such materials, or equivalently the index of refraction, changes with applied electric field, which is the so-called Pockels Effect. Unfortunately, these coefficients vanish identically for silicon because of the inversion symmetry of the diamond lattice. This becomes obvious by observing the fact that inversion symmetry requires that the following relation be true for any electric field **E**:

$$\mathbf{P}(\mathbf{E}) = -\mathbf{P}(-\mathbf{E}). \tag{2.4}$$

Consequently, for materials with inversion symmetry, only terms of an odd power of electric field **E** will be present in the equation (1.3).

For these reasons (indirect band-gap and no linear electro-optic effect), silicon has not been the material of choice for optoelectronics. There is one effect which does exist in silicon that can be used for changing its refractive index, and devices based on this effect have been successfully demonstrated [1, 2]. This is the free-carrier effect. Using classical dispersion theory it can be shown that the changes in the index of refraction and in the absorption coefficient for silicon induced by addition of free carriers are given by [3]

$$\Delta n = -\frac{e^2\lambda^2}{8\pi^2 c^2 n\epsilon_0}\left(\frac{N_e}{m_{ce}^{*2}} + \frac{N_h}{m_{ch}^{*2}}\right), \tag{2.5}$$

and

$$\Delta\alpha = \frac{e^3\lambda^2}{4\pi^2 c^3 n\epsilon_0}\left(\frac{N_e}{m_{ce}^{*2}\mu_e} + \frac{N_h}{m_{ch}^{*2}\mu_h}\right), \tag{2.6}$$

respectively, where e is the electronic charge, λ is the optical wavelength, n is the refractive index of pure silicon, ϵ_0 is the permittivity of free space, N_e and N_h are the free electron and hole densities, m_{ce} and m_{ch} are the conductivity effective masses of electrons and holes, and μ_e and μ_h are the electron and hole mobilities. Plotted in Figure 2.1 are the changes in refractive index and absorption coefficient in silicon

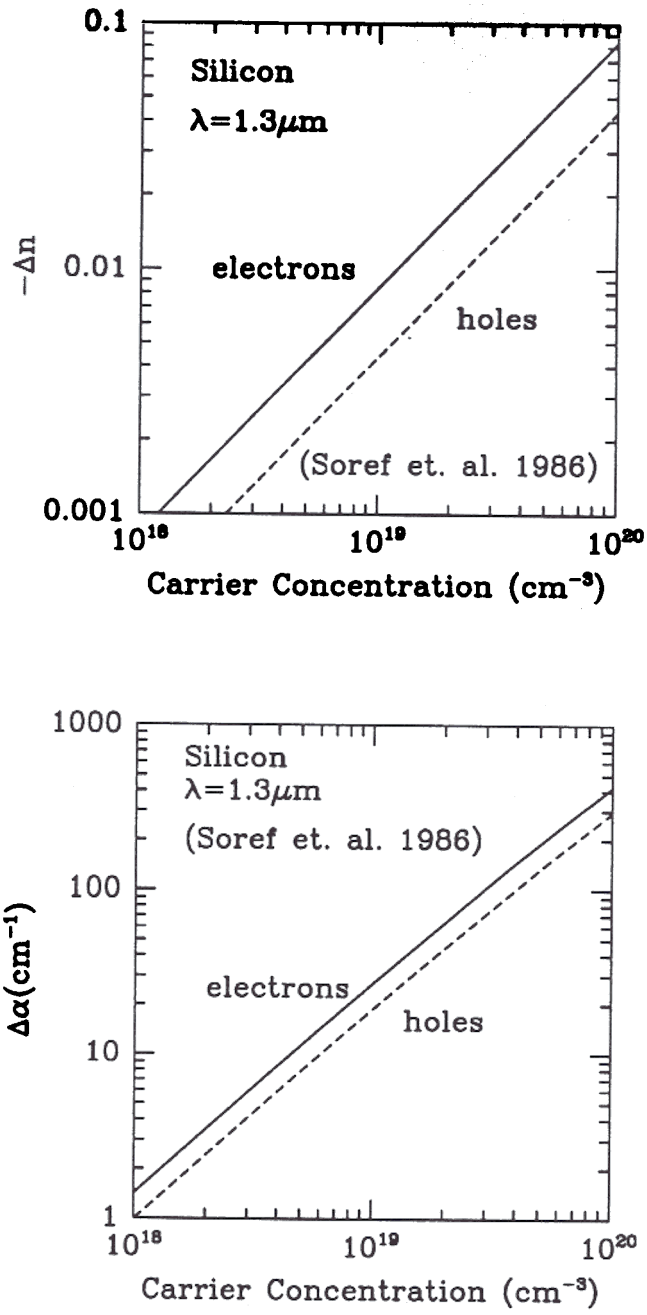

Figure 2.1: Changes in refractive index and absorption in silicon versus carrier concentration as calculated from Eqn 2.5 & 2.6.

versus carrier density as calculated from Equation 2.5 & 2.6 using $n = 3.5$, $m^*_{ce} = 0.26m_0$ (m_0 is the free electron mass), $m^*_{ch} = 0.5m_0$, and density dependent mobility data from Sze[4]. With an injected carrier density of $5 \times 10^{18}\text{cm}^{-3}$, a refractive index change of $\sim 0.5 \times 10^{-2}$ can be obtained. This is a small but adequate amount for device operation, it translates into a phase change of π over a distance of 130μm at a wavelength of 1.3μm.

In order to make an active device in silicon using free-carrier effects, it is necessary to inject carriers into and get carriers out of an active silicon region in a controlled manner. Either an optical approach, in which short wavelength light with photon energy above the silicon bandgap excites electron-hole pairs in the active region, or an electrical method, in which a forward biased p-i-n diode provides the carrier injection, can be employed to modulate the refractive index of silicon. To make an electrically controlled device, carrier injection by a p-i-n diode was used in our work.

Having chosen a physical effect for modulating the index of refraction of silicon, the next task is to design a device structure to convert the phase-modulation (due to modulation of the index) to intensity-modulation. This conversion can be achieved with many different device structures, such as directional couplers, Mach-Zehnder interferometers, etc. In our design, a Fabry-Perot resonant cavity was used for this purpose. It is much more efficient compared to the earlier approach of Hemenway *et al.*[2, 5]. The details are discussed in the following section.

2.2 Fabry-Perot Resonant Cavity

The Fabry-Perot cavity, named after its inventors Charles Fabry and Alfred Perot, is of considerable importance in modern optics. In its simplest form, the device consists of two parallel reflecting surfaces separated by some distance d. Its operation is based upon multiple-beam interference which produces very sharp resonant features. As an

example, consider a cavity formed by two mirrors of reflectivity R_m separated by a medium of refractive index n and thickness t. The reflectance and transmittance of this cavity at normal incidence are given by

$$R = \frac{4R_m/(1-R_m)^2 sin^2(\delta/2)}{1+4R_m/(1-R_m)^2 sin^2(\delta/2)} = \frac{F sin^2(\delta/2)}{1+F sin^2(\delta/2)} \tag{2.7}$$

$$T = \frac{1}{1+4R_m/(1-R_m)^2 sin^2(\delta/2)} = \frac{1}{1+F sin^2(\delta/2)} \tag{2.8}$$

where $\delta = 4\pi nt/\lambda$, and $F = 4R_m/(1-R_m)^2$ is the coefficient of finesse. These results are plotted in Figure 2.2. When the two-way optical path length ($L = 2nt$) is a multiple of the wavelength λ ($L = 2nt = m\lambda$, where m is a integer), constructive interference occurs in the cavity, and consequently, the transmittance at resonance reaches the peak value of 100% for a symmetric non-lossy cavity.

A careful look at Figure 2.2 reveals that while the response away from resonance of a high-finesse Fabry-Perot cavity is insensitive to phase changes, both the reflectance and transmittance change very rapidly with optical phase δ near resonances. These sharp features in the response of a high finesse Fabry-Perot cavity provide a very efficient mechanism for converting optical phase modulation into intensity modulation. This can be done by placing the phase modulator inside the Fabry-Perot cavity, and operating at a wavelength near one of the resonances. This device idea for making an optical intensity modulator is shown in Figure 2.3. The advantage of this configuration becomes very clear as we compare it to a conventional Mach-Zehnder type modulator, which is based upon two-beam interference (Figure 2.4) instead of multiple-beam interference as in the FP cavity. The response of the Mach-Zehnder modulator is given by

$$\frac{I_{out}}{I_{in}} = cos^2(\delta/2) \tag{2.9}$$

where δ is the optical phase difference between the two arms of the interferometer. In contrast to the FP cavity which has sharp resonant features, the Mach-Zehnder

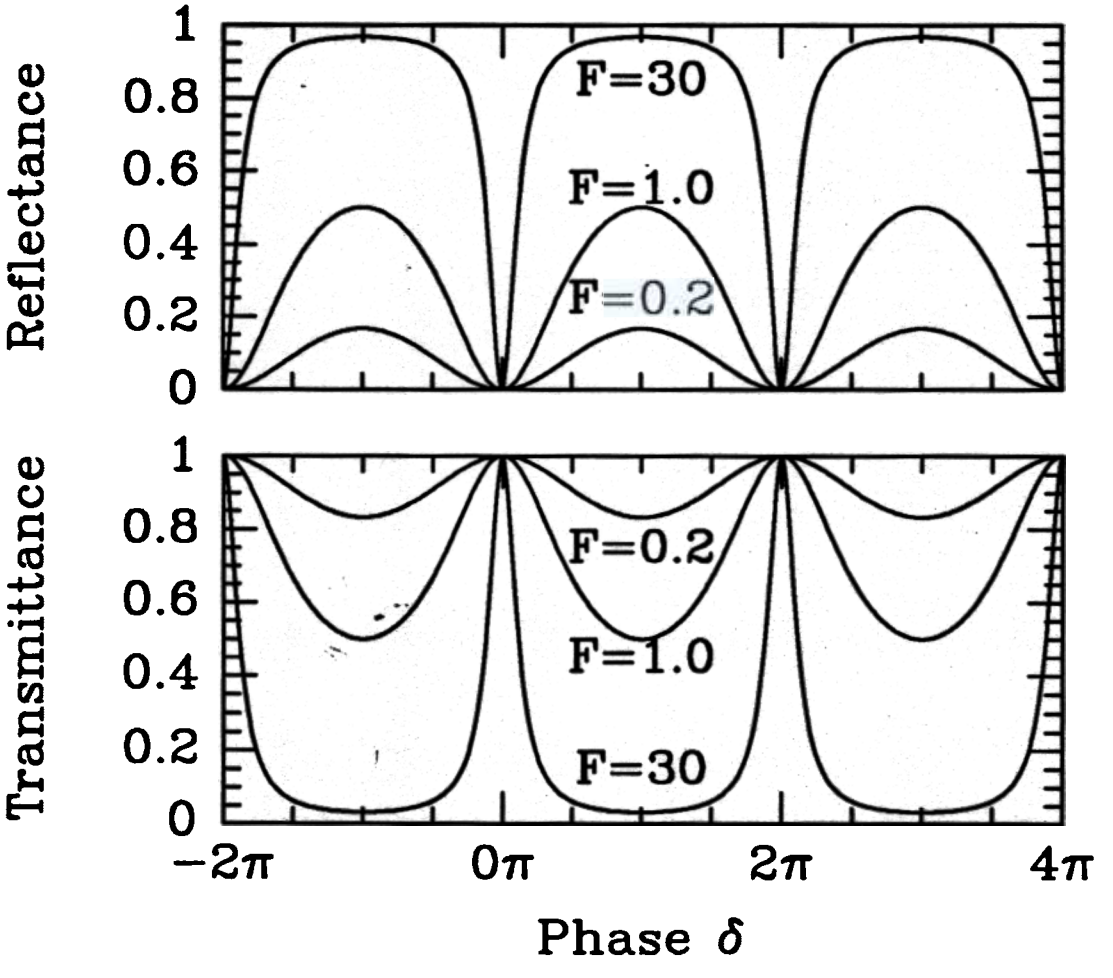

Figure 2.2: Reflectance and transmittance of Fabry-Perot cavities

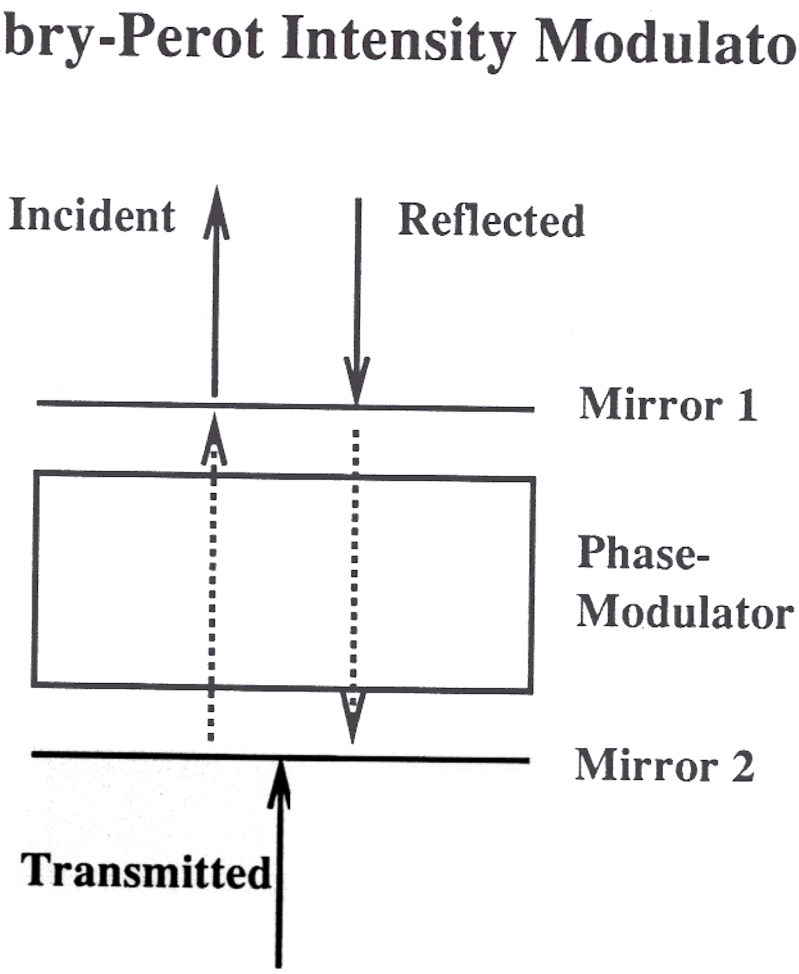

Figure 2.3: Schematic diagram of a Fabry-Perot intensity modulator.

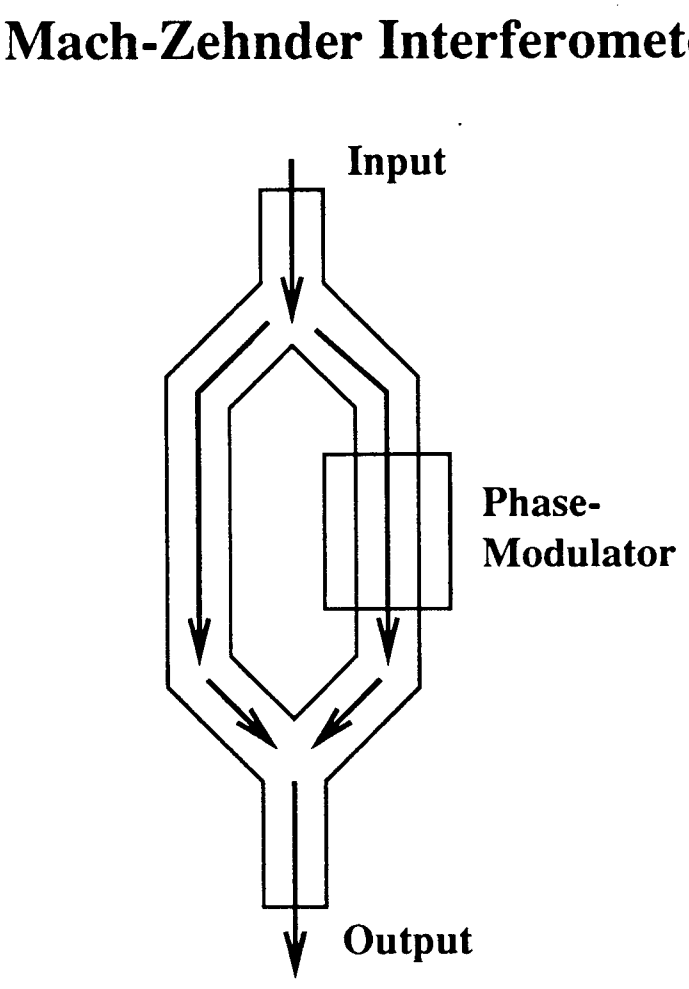

Figure 2.4: Schematic diagram of a Mach-Zehnder interferometer.

interferometer has a much "softer" response to phase changes. The derivative of the output with respect to the phase $|\frac{dI_{out}}{d\delta}|$ reaches its maximum at $\delta = (n + 1/2)\pi$, and the output of the Mach-Zehnder modulator is most responsive to changes in phase δ at these points. Very often a Mach-Zehnder device is biased at one of these points[2]. Comparing these two devices, as shown in Figure 2.5, it is obvious that by properly chosing its operating point, the FP modulator can provide a much larger intensity modulation than the Mach-Zehnder interferometer for an given phase modulation because of the much bigger $|\frac{dI_{out}}{d\delta}|$ available near its resonances.

The increased modulation depth achievable with a Fabry-Perot cavity, however, does not come without its costs. In fact, we have traded optical bandwidth for high modulation depth. The response of a FP modulator is very sensitive to operating wavelength. In order to obtain the highest performance from the FP modulator, it must be operated at a wavelength which is very close to resonance, and the light source must be monochromatic with a line width much smaller than the width of the pass-band of the FP cavity. It should be emphasized that the modulation depth will be significantly degraded if a wavelength other than the optimum value is used or if the line width of the light source is broad. Fortunately, this requirement can be easily met by using a semiconductor laser-diode, which is widely available, as a light source.

The principle of the Fabry-Perot cavity also allows us to make a highly reflective mirror in silicon using a buried oxide layer. At 1.3μm, the wavelength of interest, silicon has an index of refraction of 3.50, and the oxide 1.46. The reflectivity of a Si/SiO_2 interface is given by

$$R_{Si/SiO_2} = \frac{(n_{Si} - n_{SiO_2})^2}{(n_{Si} + n_{SiO_2})^2} = 0.17, \tag{2.10}$$

which is very low. In a $Si/SiO_2/Si$ sandwich structure, which forms a Fabry-Perot cavity itself, the reflection can be greatly enhanced, however. From Equation 2.7 the

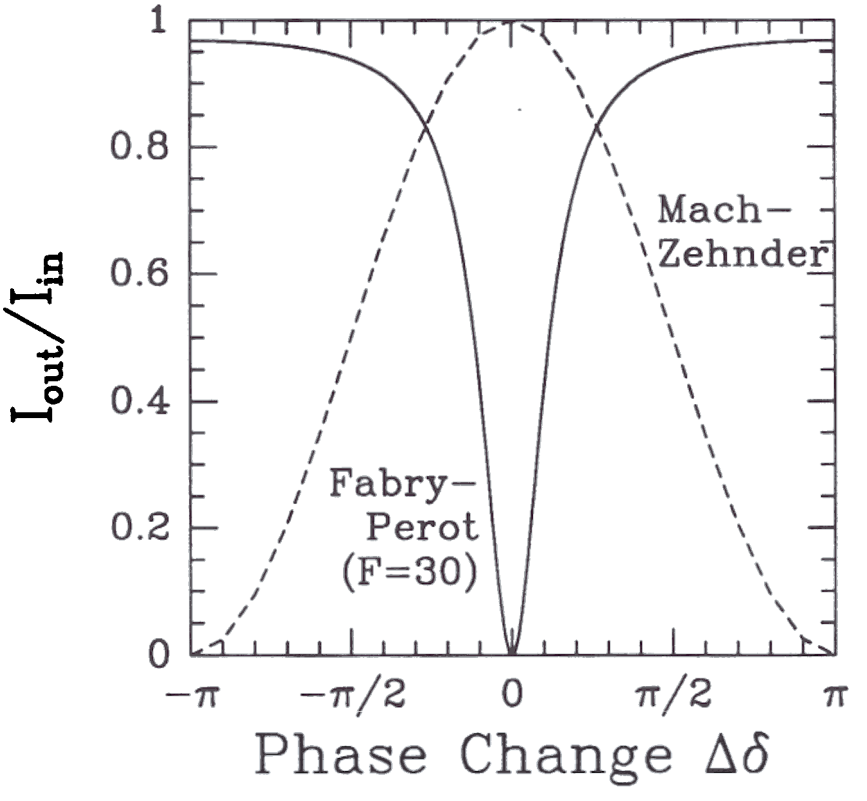

Figure 2.5: The FP modulator can provide much larger intensity modulation than the Mach-Zehnder interferometer for given phase modulation because of the bigger $dI_{out}/d\delta$.

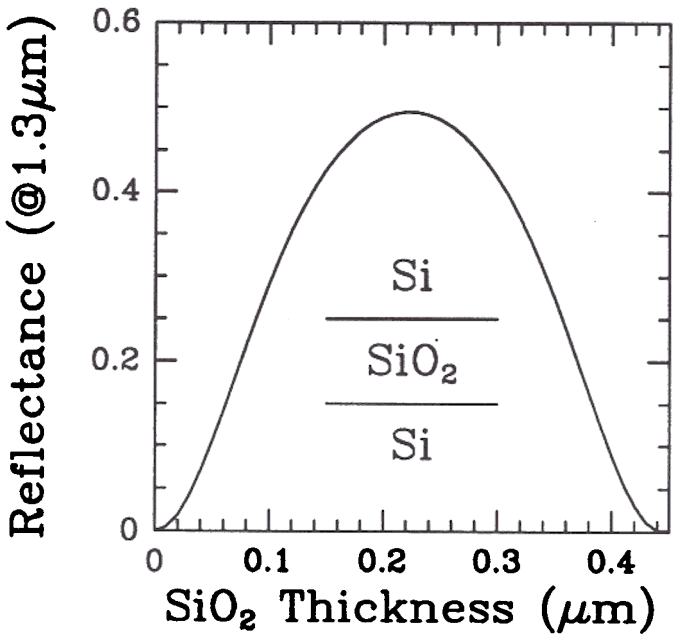

Figure 2.6: Making a mirror using a $Si/SiO_2/Si$ sandwich structure.

reflectance of the $Si/SiO_2/Si$ structure is given by

$$R_{Si/SiO_2/Si} = \frac{0.98 sin^2(1.46 \times t_{ox} \times 2\pi/1.3)}{1 + 0.98 sin^2(1.46 \times t_{ox} \times 2\pi/1.3)} \tag{2.11}$$

where t_{ox} is the oxide thickness in μm. It reaches a maximum of 0.50 for an oxide thickness of 0.22μm (Figure 2.6). The reflectance of such a structure can be further increased by employing multiple oxide layers. With a double-oxide structure, a maximum reflectance of 89% could be obtained, and a triple-oxide structure would give a maximum reflectance of 98%. Because of process constraints, a single-oxide structure was used in the devices fabricated.

Modulator Structure and Fabrication

In previous sections, we have discussed a way to modulate the refractive index of silicon, a method to convert phase-modulation into intensity modulation using a high finesse Fabry-Perot cavity, and how to make a highly reflective mirror in silicon using a $Si/SiO_2/Si$ structure. In this section, the final design of the device will be given along with a detailed description of the process steps used to fabricate such a device.

The schematic diagram of the Fabry-Perot optical intensity modulator is shown in Figure 2.7. It essentially consists of a p-i-n diode placed inside a vertical high finesse Fabry-Perot cavity formed by two $Si/SiO_2/Si$ multi-layer structures. The 0.2μm buried-oxide layer is the bottom mirror of the FP cavity, while the air/polysilicon/oxide/Si structure forms the top mirror. The p-i-n diode is mesa isolated, and metal contacts are made to both the top p+ and bottom n+ layers.

Since the device calls for a buried-oxide layer for its bottom mirror, a SIMOX (Separation by IMplantation of OXygen) wafer was used as the starting substrate for device fabrication. The total oxygen dose is $1.0 \times 10^{18}cm^{-2}$, which gives a buried-oxide layer thickness of 0.2μm. This is chosen for maximum reflection at 1.3μm. The SIMOX layers were implanted and annealed at Texas Instruments, Inc. before being sent to Princeton [6]. A structure with multiple buried oxide layers would be much better, but it would be difficult to fabricate and is not practical at the present time. The epitaxial p-i-n diode layers were grown by Rapid Thermal Chemical Vapor Deposition (RT-CVD). The p+ and n+ layers were 0.9μm and 1.4μm, respectively, and the intrinsic layer in between was about 4.0μm thick. Maximum doping levels were used in the p+ and n+ layers for efficient carrier injection into the intrinsic region. Due to background doping effect in the reactor, the undoped layer layer is normally lightly n-type doped with a concentration $\sim 1 \times 10^{16}cm^{-3}$. The growth details are given in Table 2.1.

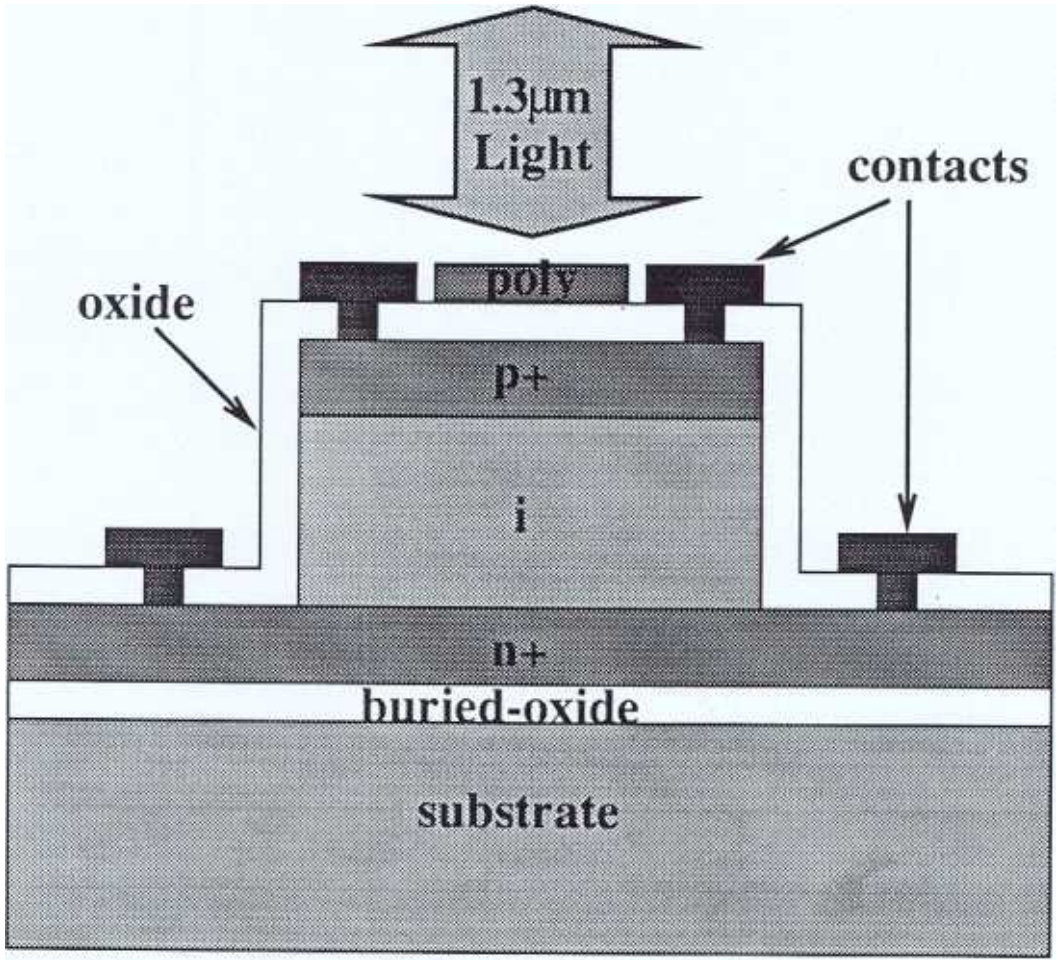

Figure 2.7: Schematic diagram of the Fabry-Perot optical intensity modulator.

Layer	Thickness μm	Time (mm:ss)	Temp. (°C)	Pres. (torr)	H_2 (slpm)	SiH_2Cl_2 (sccm)	B_2H_6 (sccm)	PH_3 (sccm)
P+	1.0	5:00	1000	6.0	3.0	26	500	–
i	4.4	22:00	1000	6.0	3.0	26	–	–
N+	1.5	8:00	1000	6.0	3.0	26	–	500

Table 2.1: Epitaxial growth conditions of the Fabry-Perot modulator.

Following the epitaxial growth, the first photolithography defines the p-i-n diode mesa. Reactive-ion-etching (RIE) was used to etch down to the heavily doped n+ layer for contact. After stripping off the photo-resist, a 2000Å thermal oxide was grown at 900°C in a wet O_2 ambient. This oxide layer functions as the top mirror of the Fabry-Perot cavity and as an electrical isolation/passivation layer. To complete the Fabry-Perot cavity, a 1000Å polysilicon layer was deposited on top of the oxide by electron-beam evaporation and the wafer was annealed for 30 minutes at 850°C in a nitrogen ambient. A second lithography step then defines optical windows on top of the diode mesas for light input and output coupling, and the polysilicon elsewhere was etched away by RIE. The reflectivity of the top air/poly/SiO_2/Si multilayer structure was calculated to be 85%. A third lithography step opens contact holes in the thermal oxide, both on top of and off the mesas. Finally, aluminum was evaporated and patterned for contact electrodes.

2.4 Device Characteristics

Electrically, the modulator is a p-i-n diode. Shown in Figure 2.8 is the I-V characteristics for a typical device. The diode shows a forward turn-on slop of ~66 mV/decade which corresponds to an ideality factor of 1.1. The series contact resistance at high current levels is less than 20Ω. The reverse leakage current of the device is below 10pA, and the breakdown voltage is about 25V, which is consistent with a background doping level of $\sim 1 \times 10^{16}\text{cm}^{-3}$ obtained from C-V measurement.

The optical cavity of the device was characterized by measuring the transmission of light through the sample as a function of wavelength using a Fourier Transform Infrared (FT-IR) spectrometer, and the results are plotted in Figure 2.9(a). As expected, the transmittance shows periodic oscillations in wave number. From the oscillation period, a silicon layer thickness of 6.20μm was obtained, which is in good

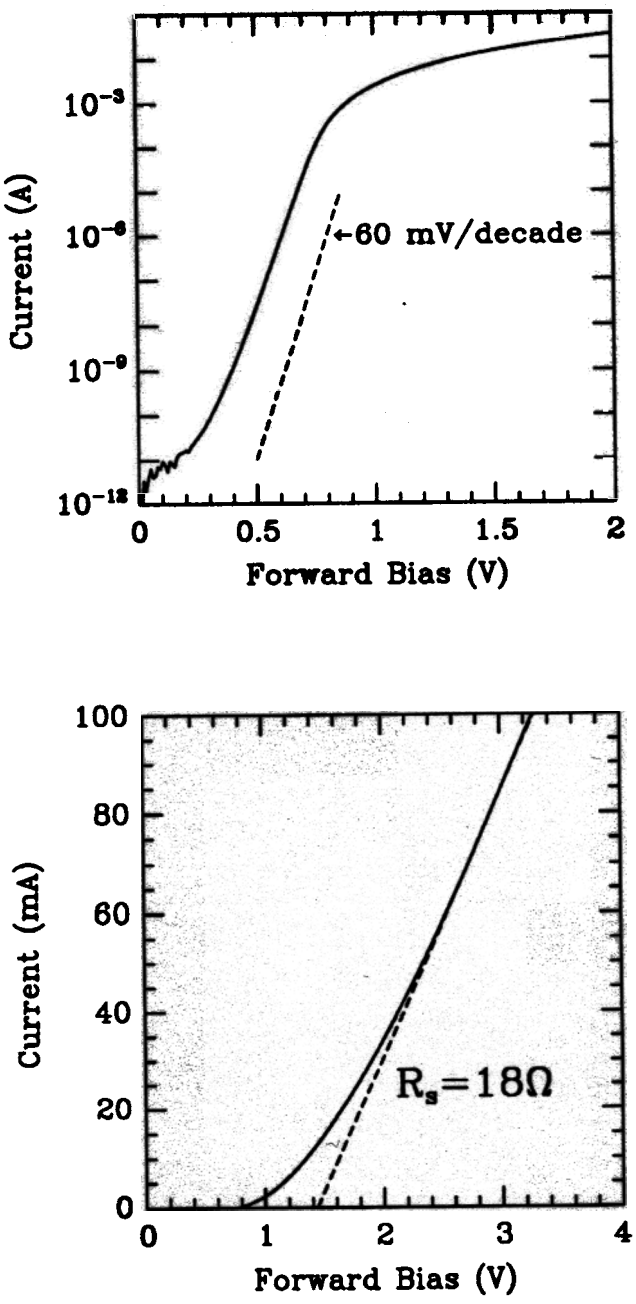

Figure 2.8: Current-voltage characteristics of a Fabry-Perot modulator.

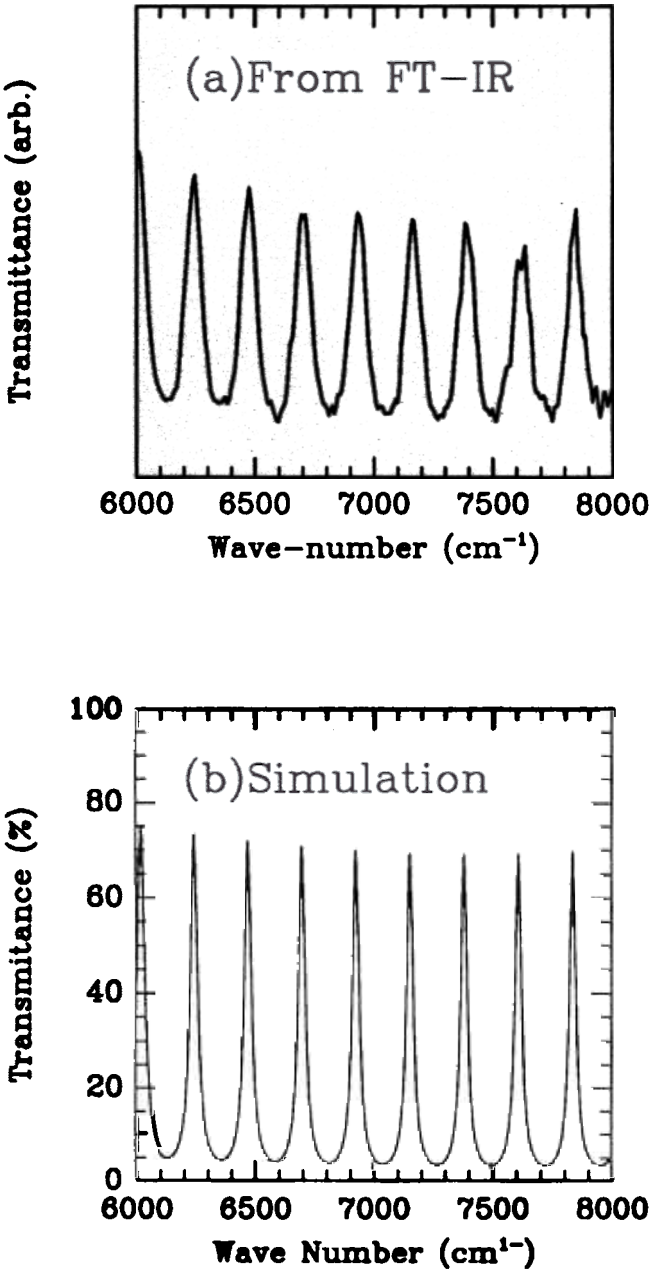

Figure 2.9: Transmittance of the Fabry-Perot modulator obtained by (a) FT-IR and (b) calculation.

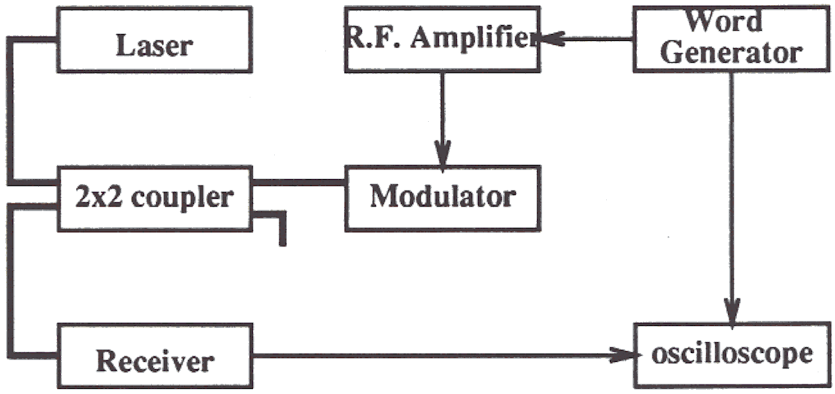

Figure 2.10: Schematic diagram of the optoelectronic measurement setup.

agreement with that measured by the bevel-and-stain technique. The broadened line width compared to the theoretical calculation (Figure 2.9(b)) is mainly due to thickness variation over the area ($\sim$ 3mm in diameter) through which the transmittance was measured by FT-IR. Another factor which may have contributed to the broadened resonances is that the light beam incident on the sample was not collimated. Nevertheless, the Fabry-Perot cavity effect was evident.

For high frequency optoelectronic measurements the device was wire bonded and mounted on a high speed header, and driven by a RF amplifier. The optical input/output coupling to the modulator was through a cleaved single-mode fiber positioned directly above the polysilicon window at the top of the device. A semiconductor laser diode operating in the CW mode at 1.3μm was used as the light source. The incoming laser light was normally incident upon the surface of the device, the reflected light from the modulator was coupled back into the single-mode fiber, separated from the incident light by a passive directional coupler and fed into an optical receiver. Both the electrical signal driving the modulator and the output from the optical receiver were displayed on an oscilloscope. The schematic diagram of the setup is shown in Figure 2.10.

Optical insertion loss is a very important figure-of-merit for a modulator. In the

case of this reflection mode device, it is given by:

$$\text{Insertion Loss} = \quad 10 \times \log\frac{I_r}{I_{in}}(\text{dB}) \tag{2.12}$$

where I_{in} is the optical power incident on the device, and I_r is the optical power reflected back into the fiber. It can be easily obtained by measuring the light intensity coming out the modulator port and the light intensity at the receiver input port. Taking into account additional insertion loss due the the passive directional coupler, an optical insertion loss of $\sim$ 4dB was obtained for the modulator. Such a low insertion loss was expected for this device because the light was coupled through the top surface of the device. The coupling fiber can be placed very close to or even in physical contact with the Fabry-Perot cavity. This essentially eliminated the additional propagation loss which would have been incurred had the incident light traveled through the thick substrate as in back-side-coupled devices [5]

Modulation depth is another important figure-of-merit for an optical intensity modulator, and it is defined as:

$$m = \frac{I_{max} - I_{min}}{I_{max} + I_{min}} \times 100\% \quad \frac{I_{max} - I_{min}}{2I_{ave}} \times 100\% \tag{2.13}$$

While the average optical intensity I_{ave} was directly measured using an optical power meter, the modulation in the light intensity ($I_{max} - I_{min}$) was obtained from the measured AC voltage from the optical receiver and its sensitivity. The modulation depth increases with the driving current. A modulation depth of 10% has been obtained at a driving current of 170mA which corresponds to a current density of $5 \times 10^3 A/cm^2$ for a device size of $60 \times 60\mu$m. This represents a current density reduction of more than an order of magnitude compared to the device described in Reference [2] for a comparable modulation depth.

Modulation bandwidth is yet another important figure-of-merit for a modulator. For a given driving current, as the frequency is increased, the modulation depth

remains constant up to a certain frequency above which it starts to drop rapidly. The 3-dB cut-off frequency is defined as the frequency at which the modulation depth of the device is one-half the value at low frequencies. For our device, we obtained a cut-off frequency of $\sim$ 40MHz, which is comparable to best results for silicon modulators [2]. Shown in Figure 2.11 are two pictures of the oscilloscope displaying data streams sent by the modulator. The 80ns delay is caused by the long ($> 10m$) fiber connecting the modulator to the optical receiver.

The bandwidth of the device is primarily determined by the carrier recombination life time. For fast devices, a small carrier recombination life is necessary. When carrier life time is reduced, a higher current level is required to achieved the same carrier injection level and modulation depth. So there is a trade off between speed and power consumption of the device.

2.5 Discussion

There are several possible ways to further improve the performance of the device. First, the device size can be scaled down. Presently, the mesa of the p-i-n diode is 60 $\times$ 60μm, while the core size of a single-mode fiber is only 8μm. Therefore, a reduction by more than an order of magnitude in device area and hence driving current should be possible. Second, the finesse of the Fabry-Perot cavity can be increased, and the two mirrors can be made more symmetrical. In the present device, the bottom mirror of the cavity is formed by a single layer of buried oxide, which has a reflectivity of only 50%. The top mirror, on the other hand, has 85% reflection at 1.3μm. Due to this asymmetry, the reflectance of the cavity can not reach down to zero even at exact resonance, and this has an adverse effect on the achievable modulation depth. By using a double buried-oxide structure, a symmetric cavity can be obtained. At the same time the finesse will be about three times higher than the

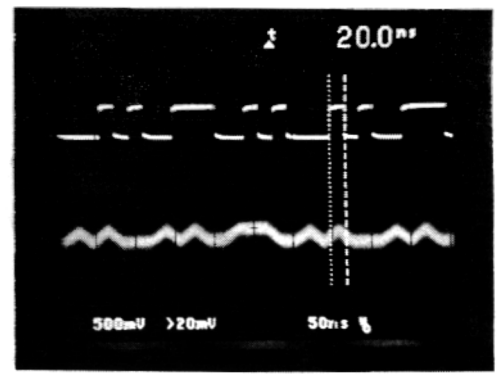

(a)

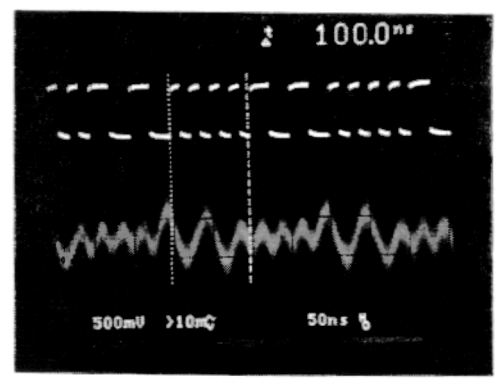

(b)

Figure 2.11: Oscilloscope picture for Not-Return-to-Zero bit rate of (a) 50 Mbits/sec, and (b) 80 Mbits/sec. The upper trace is the transmitted data. The lower trace is the output from the optical receiver. Notice an ~80ns delay in the lower traces due to a long fiber cable.

current value of 7, which means even higher modulation depth can be achieved.

The biggest drawback of this device is that it consumes much power. Unlike devices using the electro-optic effect, which only dissipate power during switching, devices based on free-carrier-effects consume power even in steady state. This is simply because a current flow is necessary to maintain a certain level of carrier injection in a free-carrier device, while no current flow is needed to keep a constant electric field in an electro-optic device. For a free-carrier device operating at 1GHz frequency, the carrier life time has to be 0.2ns or less. Even in an ideal case, to maintain an injection level of $5 \times 10^{18}/\text{cm}^3$ in an active device volume of $10 \times 10 \times 4\mu$m, the total power dissipation would be about 1W, which corresponds to a power-bandwidth-ratio of 1mW/MHz. This is an order of magnitude higher than that of typical $LiNbO_3$ or III-V compound semiconductor based devices[7].

In summary, a novel all-silicon optical intensity modulator operating at 1.3μm has been demonstrated. It had a modulation depth of 10% at a driving current density of $5 \times 10^3 \text{A/cm}^2$, an insertion loss of 4dB, and a 3-dB cut-off frequency of 40MHz. While this type of device may be useful in some moderate bandwidth applications such as a fiber-to-home return link where low cost is very desirable, devices based on free-carrier effects are not very attractive for high-speed and high-density applications where a high on-off ratio and low power consumption are required, such as high-bit-rate data links, optical computing, etc..

Chapter 3

Introduction to $Si_{1-x}Ge_x$ Alloys

In Chapter 2, pure silicon was shown to have limited potential in optoelectronics. Recently there has been tremendous interest in $Si_{1-x}Ge_x$ alloys for high-speed heterojunction electronic devices as well as for potential optoelectronic devices. The bandgap of $Si_{1-x}Ge_x$ alloys spans over a range which includes both 1.3μm and 1.55μm, two very important wavelengths in fiber optical communication. It has also been proposed that efficient light emission may be possible in zone-folded short-period Si/Ge atomic layer superlattices. Therefore, we examine $Si_{1-x}Ge_x$ alloys for potential optoelectronic applications. In this chapter, a brief introduction to strained $Si_{1-x}Ge_x$ alloys is given.

Lattice Mismatch and the Critical Thickness

Both silicon and germanium crystalize in the diamond structure. The lattice constants of silicon and germanium are 5.43Å and 5.64Å, respectively, which translates into a 4% lattice mismatch ($\Delta a/a$) between the two. Silicon and germanium can mix at any ratio and form a homogeneous random alloy $Si_{1-x}Ge_x$, where x is the atomic fraction Ge.

When a $Si_{1-x}Ge_x$ alloy is epitaxially grown on a silicon substrate, there are two mechanisms to accommodate the lattice mismatch. In one case, misfit dislocations

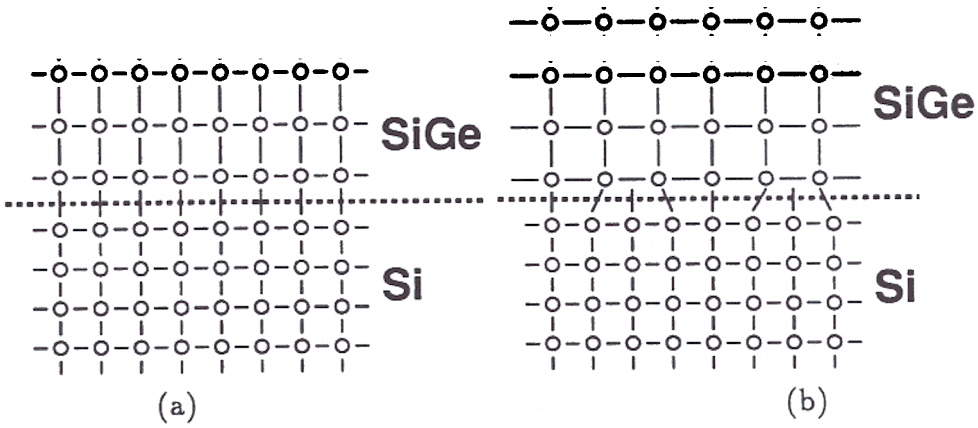

Figure 3.1: Acommodation of lattice mismatch by (a) strain, and (b) misfit dislocations.

are generated at the interface. A misfit dislocation is essentially an extra half-plane of atoms in the silicon substrate which is not matched by atoms in the $Si_{1-x}Ge_x$ epitaxial film(Figure 3.1 (b)). The dangling bonds associated with the misfit dislocations are very efficient carrier generation and recombination sites, and films full of misfit dislocations generally have very low minority carrier recombination lifetime. Therefore misfit dislocations are detrimental to minority carrier devices such as heterojunction bipolar transistors (HBT's), as well as optical devices like light-emitting diodes (LED's). Alternatively, the lattice mismatch can be accommodated by coherent strain in the $Si_{1-x}Ge_x$ alloy film. In this case, the $Si_{1-x}Ge_x$ alloy film takes an in-plane lattice constant matched to that of the silicon substrate, and as a result, the lattice is elongated in the growth direction (Figure 3.1 (a)). In coherently strained growth, there is no generation of misfit dislocations. Therefore, it is desired over misfit dislocations for the lattice misfit accommodation.

From thermodynamic considerations, for a small lattice mismatch, it is energetically more favorable for the system to remain coherently strained and free of misfit dislocations when the $Si_{1-x}Ge_x$ film is sufficiently thin. As the film thickness increases above a certain value, however, the energy associated with the homogeneous strain

in the film will become so large that the introduction of misfit dislocations will be favored, and this layer thickness is the so-called critical thickness. There exist several theories on the issue of critical layer thickness [8, 9, 10]. Most noteworthy was the mechanical equilibrium theory of Mathews and Blakeslee [9]. In their theory, the critical thickness is the thickness for which a grown-in threading dislocation becomes mechanically unstable and starts to bow and propagate to form an interfacial misfit dislocation line. According to this theory, the critical layer thickness h_c is given by

$$h_c = \left(\frac{1}{f}\right)\left[\frac{b}{4\pi(1+\nu)}\right]\left[ln\left(\frac{h_c}{b}\right)+1\right] \tag{3.1}$$

where f is the misfit ($\Delta a/a$), b is the slip distance, and ν Poisson ratio. Using a slip distance of 4Å and a Poisson ratio of 0.28, the critical layer thickness of $Si_{1-x}Ge_x$ on (001) silicon substrate as calculated from Equation 3.1 is plotted in Figure 3.2. It should be noted that Mathews and Blakeslee's theory is an equilibrium theory, which does not incorporate any kinetics of dislocation nucleation and propagation. It is possible to have a $Si_{1-x}Ge_x$ film which is above this critical layer thickness and yet remains fully strained and free of dislocations. A film with thickness above the critical value, however, is metastable, and with energy provided from other sources, such as heat, the strain will relax and dislocations will be generated in the film. As an example, the critical layer thickness for a Ge fraction of 20% is only 135Å from the theory of Mathews and Blakeslee, and dislocation free $Si_{1-x}Ge_x$ layers with thickness up to about 500Å have been successfully grown in the Rapid Thermal Chemical Vapor Deposition reactor at Princeton.

3.2 Electrical Properties

Because both are group IV elemental semiconductors, silicon and germanium have fairly similar electronic band structures. The valence band maxima of both Si and

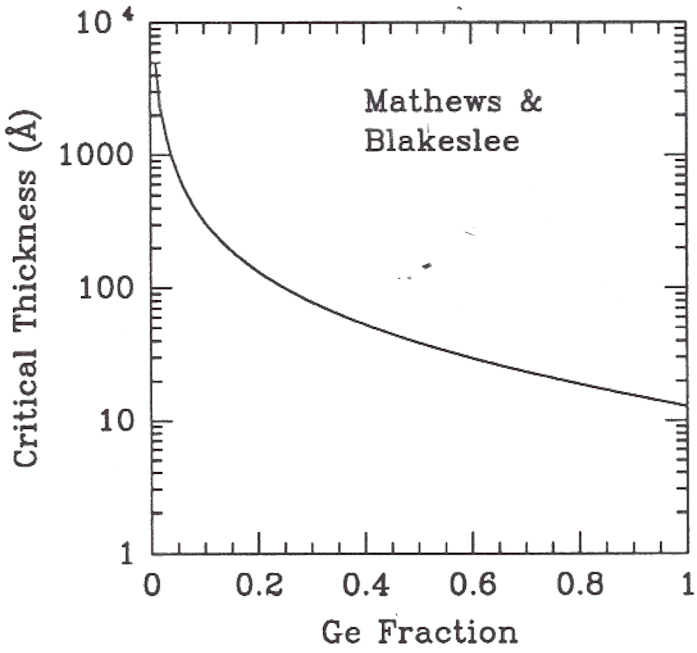

Figure 3.2: Critical layer thickness of $Si_{1-x}Ge_x$ on Si (after Mathews and Blakeslee).

Ge are located at the center of the Brillouin zone (BZ) (Γ). For silicon, a total of six conduction band minima are located along six equivalent Δ ($\Gamma - X$) axes. For germanium, the conduction band minima are located at the BZ boundary L points, and there exists a valley degeneracy of four. While silicon has a fundamental indirect bandgap of 1.17eV at zero Kelvin, germanium has a fundamental indirect bandgap of 0.66eV.

Even though the $Si_{1-x}Ge_x$ random alloy is not a crystal in the most rigorous sense, translational symmetry, nevertheless, remains a very good approximation, and the associated band structure is a valid and very helpful concept. The band structure of a bulk unstrained $Si_{1-x}Ge_x$ alloy remains silicon-like with the conduction band minima along the Δ axes for Ge fractions up to about 85%, above which the L points become the conduction band minima as in Ge. The valence band maximum remains at the Brillouin-zone center Γ, so the $Si_{1-x}Ge_x$ alloy is also an indirect bandgap semiconductor. The fundamental bandgap of bulk unstrained $Si_{1-x}Ge_x$ alloy as a function of Ge mole fraction was first measured by Braunstein [11] using an optical absorption technique, and their results are shown in Figure 3.3. The kink at $x \sim 0.85$ represents the switch from a Si-like band structure at lower Ge fractions to a Ge-like band structure at higher Ge fractions.

When $Si_{1-x}Ge_x$ is grown epitaxially on silicon with its lateral lattice constant matched to that of the silicon substrate (coherently strained), its band structure will be different from that of the bulk relaxed alloy due to strain effects. In particular, for strained $Si_{1-x}Ge_x$ alloys grown on (001) silicon, the epitaxial $Si_{1-x}Ge_x$ film is under biaxial compressive stress because of its larger unstrained lattice constant compared with that of Si substrate. The bandgap of strained $Si_{1-x}Ge_x$ on (001) silicon was first calculated by People [12] within the framework of deformation potential theory. According to the deformation potential theory, under biaxial compressive stress, four

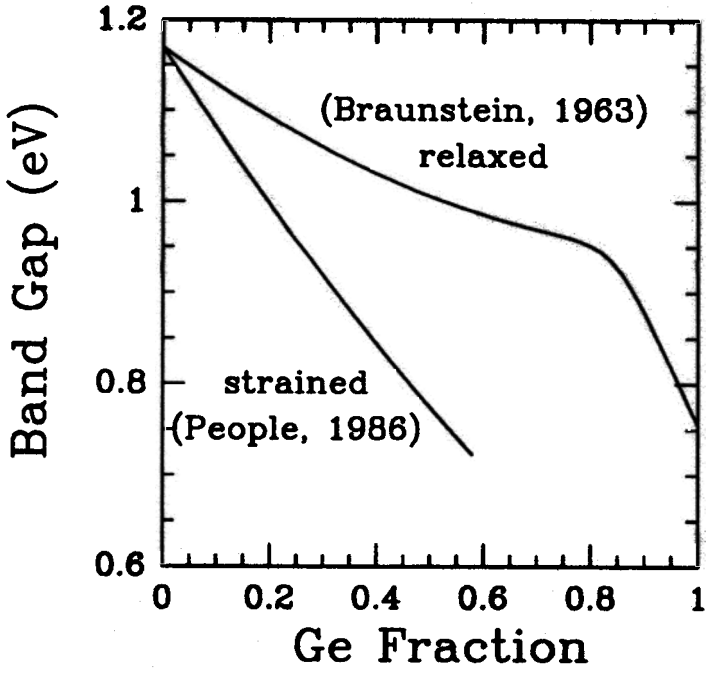

Figure 3.3: Band gap of $Si_{1-x}Ge_x$ alloys.

of the six conduction band valleys (those in the [100], [$\bar{1}$00], [010], and [0$\bar{1}$0] directions), move down with respect to the other two valleys (those in the [001] and [00$\bar{1}$] directions) becoming the conduction band minima. In the valence band, under the same stress, the four-fold degenerate Γ point splits into two two-fold bands (a heavy hole and a light hole band) with the heavy hole band being the highest lying valence band. The fundamental bandgap of coherently strained $Si_{1-x}Ge_x$ on a (001) silicon substrate as calculated by People [12] is also shown in Figure 3.3 in comparison with the bandgap of unstrained $Si_{1-x}Ge_x$ alloy as measured by Braustein. Notice that the band-gap of $Si_{1-x}Ge_x$ alloy decreases much more rapidly with increasing Ge fraction in the case of the coherently strained film on a (001) silicon substrate than in the case of unstrained bulk alloy. The bandgap of $Si_{1-x}Ge_x$ spans a range which include both 1.3μm and 1.55μm, two very important wavelengths in fiber optics, which make strained $Si_{1-x}Ge_x$ alloy a very attractive candidate for silicon based optoelectronics applications. The plot of bandgap vs. Ge fraction (Figure 3.3) gives no information about the band alignments at a $Si_{1-x}Ge_x$/Si interface, however. We will come back and focus on this issue in the next chapter.

3.3 Rapid Thermal Chemical Vapor Deposition

At Princeton we grow $Si_{1-x}Ge_x$ alloy films using the technique of Rapid Thermal Chemical Vapor Deposition (RT-CVD) [13], which is a combination of rapid thermal processing and chemical vapor deposition. A schematic diagram of the reactor at Princeton is shown in Figure 3.4. The wafer is supported by a quartz stand which sits in a quartz reactor chamber and is heated by a bank of tungsten-halogen lamps located outside the chamber. The substrate temperature is monitored *in situ* using an infrared laser transmission technique developed at Princeton [14], which is accurate to a few degrees. The source gases for Si and Ge are dichlorosilane and germane,

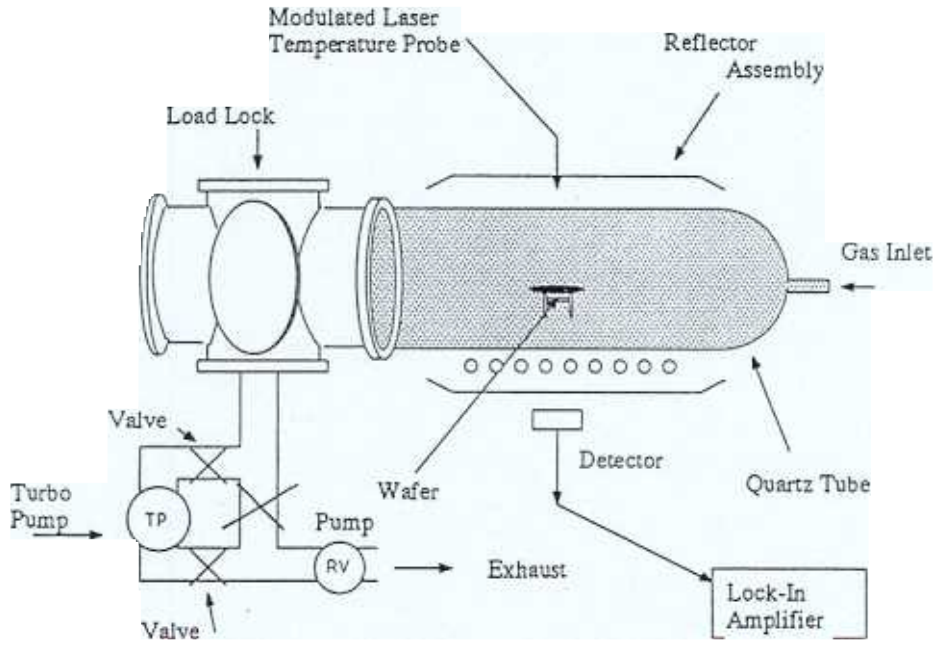

Figure 3.4: Rapid Thermal Chemical Vapor Deposition reactor at Princeton (courtesy of P. V. Schwartz).

respectively, and hydrogen is used as the carrier gas. Typical growth temperatures are 625°C for $Si_{1-x}Ge_x$ and 700°C for Si. Typical growth pressure is 6 Torr. Our reactor is not an ultra-high-vacuum system. However, in order to to ensure a high carrier life time in the epitaxial films, a load-lock is employed to eliminate oxygen and water vapor contamination which would otherwise be introduced into the chamber during wafer loading and unloading. Low oxygen content and long carrier life time films can be routinely grown at 625/700 ^oC with interface abruptness better than 1nm [15].

Photoluminescence

When a semiconductor is illuminated by a light beam with its photon energy above the band gap of the semiconductor, electron-hole pairs due to interband photo-absorption processes will be generated inside the semiconductor. These photo-excited hot carriers will very quickly relax to the conduction band minima (electrons) or valence band maxima (holes) in **k**-space by giving up their energy to the lattice through phonon emission and other scattering processes. Subsequently, these excess electrons and holes can radiatively recombine with each other and emit light as "photoluminescence". Useful information on the electronic and optical properties of the semiconductor can be extracted from its photoluminescence spectra.

Not all electron-hole recombinations result photon emission. The recombination processes of electron and hole can be classified into two categories: radiative and non-radiative recombination. As the names imply, in the radiative processes photons are emitted when electrons recombine with holes, while in the non-radiative process there is no photon emission. Both kinds of processes are always present and compete against each other. In order to observe photoluminescence from an indirect bandgap

semiconductor, the sample is required to be of high quality in terms of carrier recombination life time in order to suppress the competing non-radiative recombination processes due to deep levels or traps.

For indirect semiconductors, such as Si and Ge, direct recombination of an electrons and a hole is not allowed due to the momentum conservation requirement Radiative recombination of electrons and holes only result from second or higher order processes, such as phonon emission. In $Si_{1-x}Ge_x$ alloys, several recombination mechanisms exist which result in photon emission. These include phonon-assisted transitions, alloy-scattering-assisted transitions, and even defect-associated transitions, among others. The most important ones are the first two types which are also called band-edge luminescence because they are related to the electron states at the conduction minima and hole states at the valence band maximum.

For bulk unstrained $Si_{1-x}Ge_x$ alloys, there had been several reports of well-resolved band-edge photoluminescence, including the most comprehensive work of Weber and Alonso [16]. For strained $Si_{1-x}Ge_x$ alloy films, on the other hand, only very recently has the perfection of crystal growth techniques allowed the first observation of well-resolved band-edge photoluminescence of excitons [17, 18]. A typical PL spectrum obtained at 4K from a strained $Si_{1-x}Ge_x$ layer grown by RTCVD at Princeton is shown in Figure 3.5. It is dominated by luminescence due to shallow bound excitons [18]. It has a no-phonon (NP) transition due to alloy scattering as the highest energy component, and four monmentum conserving phonon-assisted replicas at lower energies, which are attributed to the transverse acoustic (TA) phonon replicas and to three distinct transverse optical (TO) replicas due to Ge-Ge, Ge-Si, Si-Si [16].

It should be pointed out that PL in $Si_{1-x}Ge_x$/Si structures has been observed from unknown sources with an energy well below the bandgap [19], and in "zone-folded"

[1]Luminescence in Si and Ge from bound-excitons at very low temperatures is due to localization of carriers.

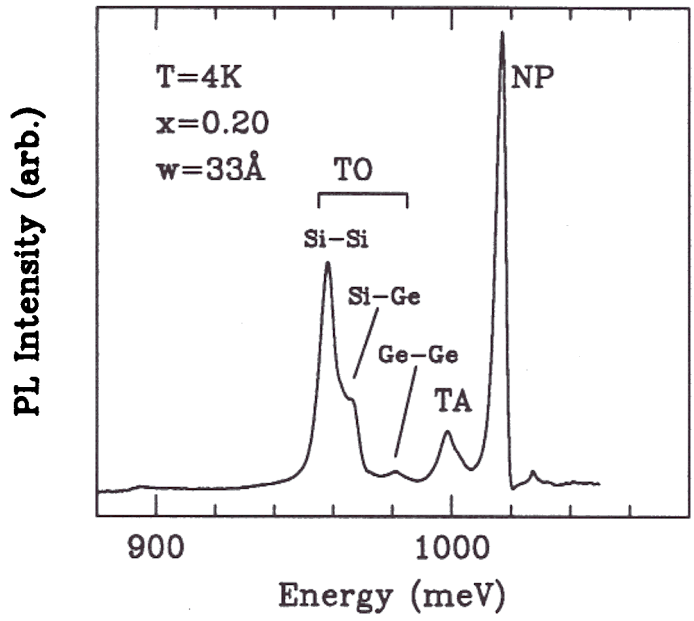

Figure 3.5: A typical photoluminescence spectrum from a $Si/Si_{1-x}Ge_x/Si$ single quantum well sample.

Si/Ge short-period superlattices [20, 21], although the "zone-folded" PL may be due to dislocations [22] and not to the superlattice itself. Our attention will be focused on the band-edge photoluminescence of strained $Si_{1-x}Ge_x$ alloys.

Chapter 4

Band Alignment of Strained $Si_{1-x}Ge_x$ on Si

4.1 Type-I vs. Type-II Band Alignment

When two different semiconductors are joined together as in a strained $Si_{1-x}Ge_x/Si$ heterojunction, there are two possible types [1] of band alignment which are depicted in Figure 4.1. In the case of type-I band alignment, the bandgap of the narrower-gap material lies entirely within the band-gap of the wider-gap semiconductor (Figure 4.1(a)). In the case of type-II alignment, the band edges of two semiconductors line up in a staggered form (Figure 4.1(b)). Two important material parameters here are the conduction band offset ΔE_c and valence band offset ΔE_v. They are related to each other through the following equation:

$$\Delta E_c + \Delta E_v = \Delta E_g \tag{4.1}$$

where ΔE_g is the bandgap difference between the two semiconductors.

Knowledge of the band alignment of the SiGe/Si heterostructure is very important for understanding its carrier transport and optical properties. It has been a subject

[1] An extreme case of type-II band alignment where the valence band edge of one semiconductor lies above the conduction band edge of the other semiconductor is sometimes referred to as type-III band alignment.

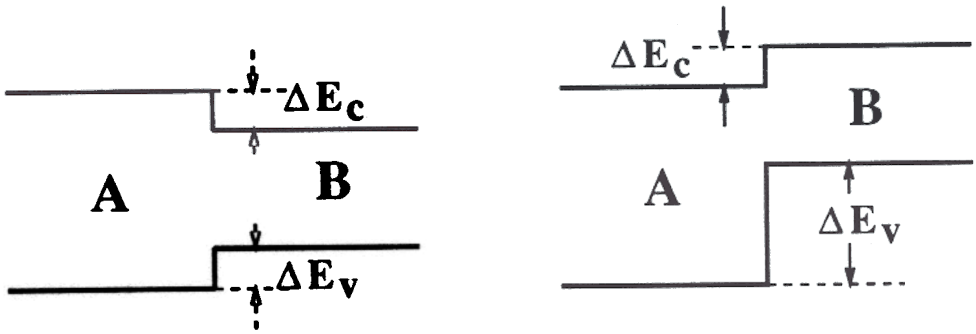

(a) Type-I **(b) Type-II**

Figure 4.1: Type-I and Type-II band alignment

of $Si_{1-x}Ge_x$ material research from the very beginning. In order to present the reader a relatively complete picture of the status of our current understanding of this issue, previous work by several groups will first be briefly reviewed.

In an early transport study of modulation-doped $Si_{1-x}Ge_x$/Si strained layer heterostructures, People *et al.*[23] found that while two-dimensional hole gases with dopant in silicon were observed in p-type doped structures with a Ge fraction of 0.20, similar n-type structures showed no sign of two-dimensional electron gases. It should be noted that at low temperatures in order to have any carrier transfer in a modulation doped structure (from the donor or acceptor level in the barrier to the 2-D channel), a minimum band offset is required. For a n-type modulation doped structure, it can be shown (Figure 4.2) that the band offset will be given by

$$\Delta E_c = E_d + \Delta\phi + E_0 + E_f \tag{4.2}$$

where E_d is the donor energy measured from the conduction band edge, $\Delta\phi$ is the total band bending in the barrier, E_0 is the first electron subband energy measured from the lower conduction band edge at the interface, and E_f is the Fermi level with respect to the 2-D band edge. Neglecting the three last terms which vanish at zero-carrier transfer, the minimum value of band offset required for the formation of a 2-D

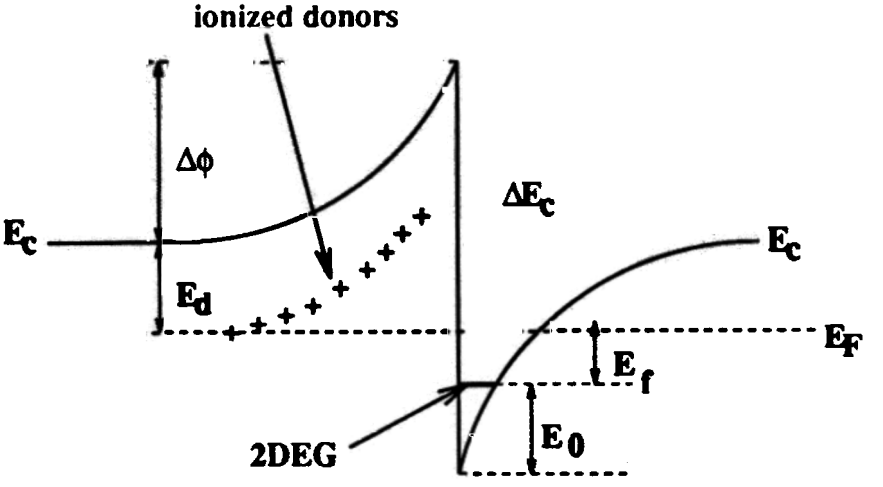

Figure 4.2: Schematic band diagram of a n-type modulation doped structure

electron gas would be E_d, which is the distance from the donor level to the conduction band edge, or the donor ionization energy. The ionization energy for a shallow donor or acceptor in silicon is typically 40meV. While a 2-D hole gas was observed in the p-type modulation doped $Si_{0.8}Ge_{0.2}/Si$ structure, indicating a substantial valence band offset ($\geq$ 50meV), the fact that no 2-D electron gas was observed only indicated that the corresponding conduction band offset is less than 40meV. In our view, this experiment did not prove nor did it rule out the possibility of a type-I alignment, in contrast to some people's belief that it indicated a type-I alignment [24].

The first observation of mobility enhancement of two-dimensional electrons confined in Si layers in Sb doped $Si_{1-x}Ge_x/Si$ superlattices was reported by Jorke and Herzog [25]. Their results indicated that the conduction band edge of Si is lower than that of strained $Si_{1-x}Ge_x$, i.e. a type-II band alignment. Later it was proposed by Abstreiter *et al.* [26] that the observed type-II alignment may be due to the biaxial tensile stress in the Si layers due to the relaxation of the $Si_{0.75}Ge_{0.25}$ buffer layer upon which the $Si_{0.5}Ge_{0.5}/Si$ superlattice was grown. While their results clearly proved a type-II alignment for $Si/Si_{0.5}Ge_{0.5}$ on relaxed $Si_{0.75}Ge_{0.25}$ buffer layer, the question of

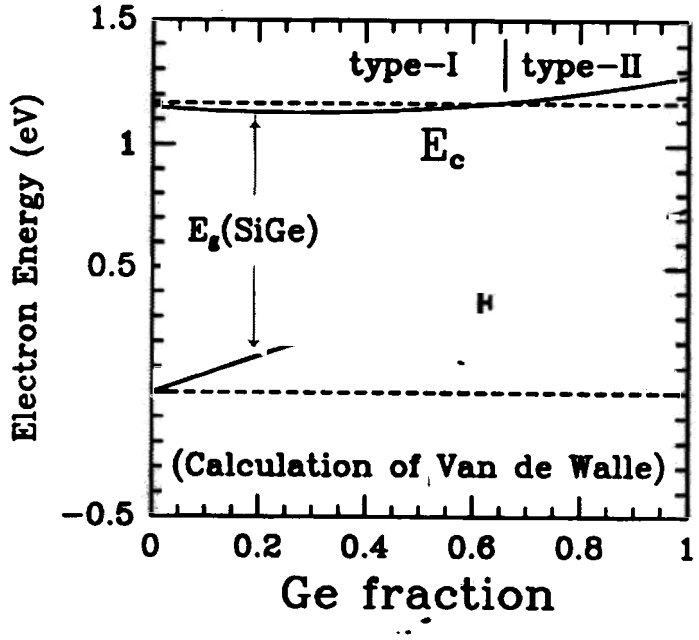

Figure 4.3: Band alignment of strained $Si_{1-x}Ge_x$ on (100) silicon as calculated by van de Walle [28].

band alignment for strained $Si_{1-x}Ge_x$ on Si was yet to be answered.

On the theoretical side, Chris van de Walle calculated the valence band alignment of the Ge/Si interface for three different lateral lattice constants within the framework of local density functional theory [27, 28] It was extended to $Si_{1-x}Ge_x$ alloys by combining the results with the phenomenological theory of deformation potentials. The results are shown in Figure 4.3. From his results, a large valence band offset ($\sim$ 90% of the total bandgap reduction) was predicted for strained $Si_{1-x}Ge_x$ on (100) silicon, which increases monotonically with increasing Ge fraction. The conduction band offset, on the other hand, remains small in the whole composition range, and it exhibits a sign change at $x \sim 0.65$, resulting in a switch from type-I to type-II alignment.

By combining the calculation of valence band offset for pseudomorphic Ge/Si interfaces by van de Walle and Martin with the strained band gap data of Lang *et al.* [29] and their calculation of the strained band gap from the deformation potential theory, People and Bean [24] have put forward their own version of the band line-up for strained $Si_{1-x}Ge_x$ on (100) silicon, which also indicates a type-I alignment for Si-rich alloys with most of the offset in valence band. It should be noted that in both calculations (van der Walle and People/Bean) of the conduction band discontinuity at the strained $Si_{1-x}Ge_x$/Si interface, linear interpolations were first used to calculate the valence band offset ΔE_v from those of Si/Ge interfaces, then deformation potential theory was used to calculate the band gap E_g of the strained $Si_{1-x}Ge_x$ alloy, and finally the conduction band offset was calculated using Equation 4.1. Given the fact that some of the parameters needed in these calculations are not accurately known even for pure Si and Ge, and that additional interpolation had to be used to calculate these parameters for $Si_{1-x}Ge_x$ alloy, there are some uncertainties in these theoretical results.

In the past few years, many experiments have been performed to measure the band alignment. Most of these studies focused on the valence band offset [30, 31] and the total band gap reduction [29, 32]. At present, it is widely accepted that the band gap of strained $Si_{1-x}Ge_x$ decreases with increasing Ge fraction much faster than that of the unstrained alloy, and that most of the band gap reduction occurs as a positive valence band offset (E_v of $Si_{1-x}Ge_x$ lies higher than that of Si). While the experimental data in general agree well with the theories of van der Walle and People/Bean, a sizable variation (> 20 meV) in the value of ΔE_v and ΔE_g remains. Although it is agreed that the magnitude of the conduction band offset is small for $x \leq 0.40$, the sign of band offset in the conduction band at the strained $Si_{1-x}Ge_x$/Si interface is still in dispute. For example, using optically detected magnetic resonance (ODMR) of photoluminescence from a Si/$Si_{1-x}Ge_x$ strained-layer superlattice, Glaser

et al.[33] suggested a type-II band alignment for x=0.35. This was based on the fact that the resonance features they observed in a $Si_{0.65}Ge_{0.35}/Si$ superlattice had a g value of 1.998 ± 0.001 which was consistent with that of either electrons or shallow donors in Si. They could not, however, rule out the possibility of a type-I alignment [33].

Because of the uncertainty in the sign of the conduction band offset, it is clear that more direct experimental evidence is needed to definitively establish the type of band alignment for strained SiGe on (001) silicon. In this section, we present direct evidence we have obtained from a comparative study of band-edge photoluminescence from strained $Si/Si_{1-x}Ge_x/Si$ single well and $Si/Si_{1-y}Ge_y/Si_{1-x}Ge_x/Si_{1-y}Ge_y/Si$ stepped well structures which unambiguously indicates that the conduction band edge of strained $Si_{1-x}Ge_x$ with $x \leq 0.35$ on (100) silicon is **not** above that of unstrained Si, proving a type-I band alignment. Measurements of ΔE_v by internal photoemission spectroscopy are then combined with photoluminescence measurements on the same samples (measuring E_g) to experimentally determine ΔE_c vs. x.

4.2 Single Well vs. Stepped Well

As noted in the previous chapter, for a bulk sample, the band edge photoluminescence energy provides a very accurate measure of the energy band gap of the material. For a strained $Si/Si_{1-x}Ge_x/Si$ well, however, the photoluminescence energy may not necessarily reflect the band gap of the $Si_{1-x}Ge_x$ layer because of a possible type-II spatially indirect transition in the structure.

It is important to keep in mind that at low temperatures, such as 4K which corresponds to a thermal energy kT of less than 0.4meV, most photoexcited carriers will relax to the lowest energy position. The band-edge photoluminescence

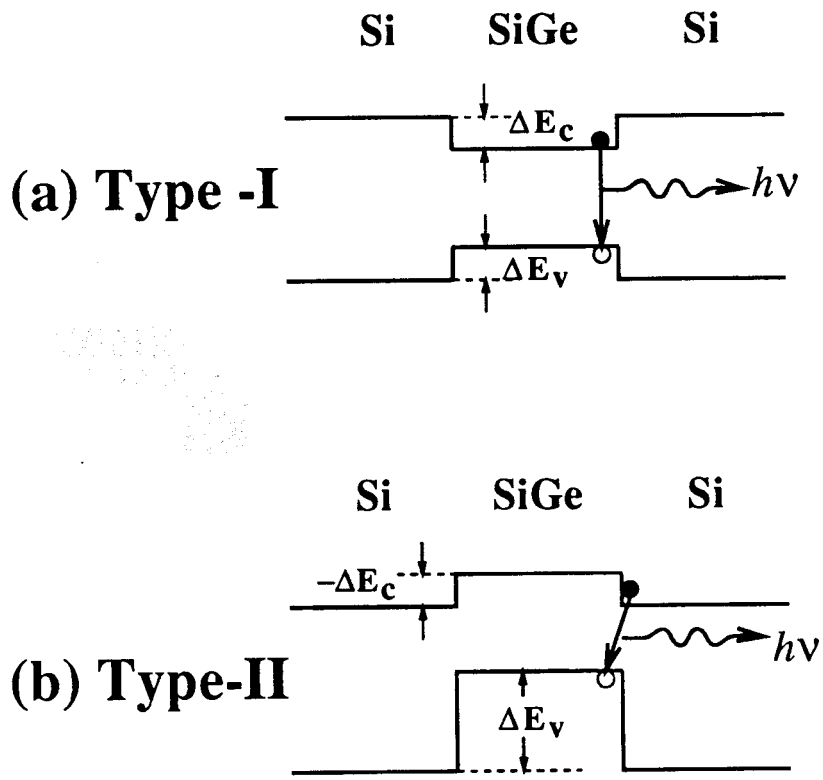

Figure 4.4: Type-I (a) and type-II (b) recombination in a $Si/Si_{1-x}Ge_x/Si$ single well.

energy thus provides a very accurate measure of the relative positions of the conduction band and valence band edges from where the electron-hole recombination takes place. In a $Si/Si_{1-x}Ge_x/Si$ single well (SW) structure, if the band alignment is type-I, at low temperatures the photoluminescence will be due to recombination of electrons and holes all in the strained $Si_{1-x}Ge_x$ layer (Figure 4.4 (a)). If the band alignment is type-II, on the other hand, the PL will be due to recombination of electrons in the Si layer with holes in the $Si_{1-x}Ge_x$ well (Figure 4.4 (b)). While in the first case (spatially direct, or type-I), the PL energy reflects the band gap of the strained $Si_{1-x}Ge_x$ layer, in the second case (spatially indirect, or type-II) it does not. These two cases can be distinguished by introducing a $Si_{1-y}Ge_y$ ($y < x$) cladding layer on each side of the original $Si_{1-x}Ge_x$ layer in a stepped well (STW) structure (

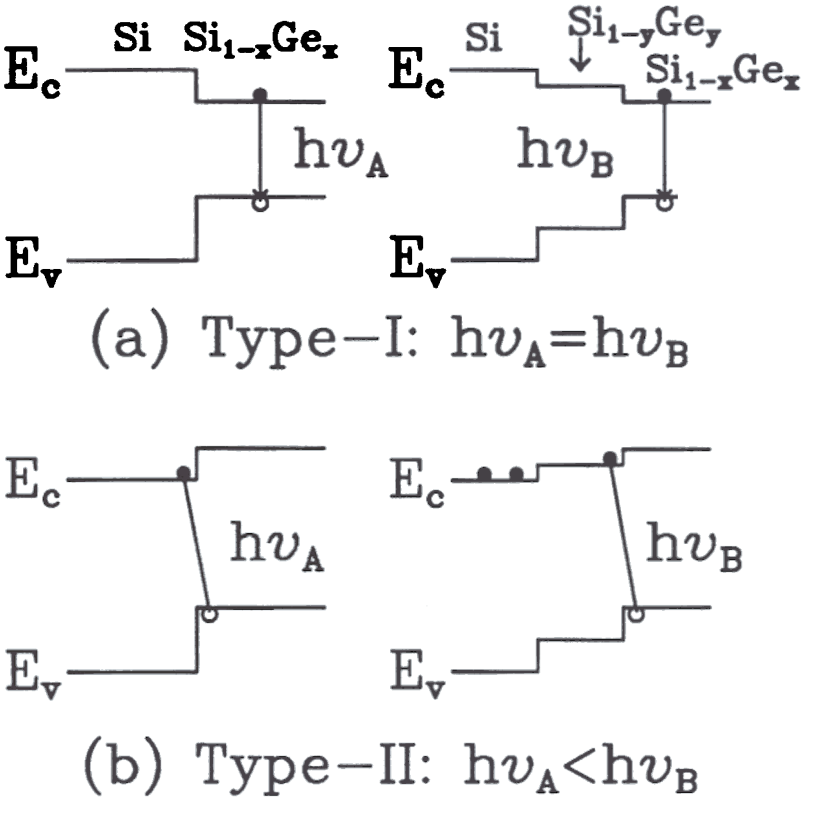

Figure 4.5: Recombination in single wells and stepped wells. (Because of the symmetry, only half of the band diagrams are shown.)

$Si/Si_{1-y}Ge_y/Si_{1-x}Ge_x/Si_{1-y}Ge_y/Si$) and comparing the photoluminescence energies of the SW and STW samples.

The differences in recombination processes between SW structures and STW structures are shown schematically in Figure 4.5. The sign of the conduction band (CB) offset ΔE_c was determined by comparing photoluminescence(PL) in the two types of structures. If the alignment is type-I, the observed PL energy of the STW structure will be the same as that of the single well (SW) structure since the holes and electrons

Sample #	Structure	Well Thickness	Cladding Thickness
1007	$Si/Si_{0.80}Ge_{0.20}/Si$	200Å	N/A
1006	$Si/Si_{0.85}Ge_{0.15}/Si_{0.80}Ge_{0.20}/Si_{0.85}Ge_{0.15}/Si$	200Å	200Å
1049	$Si/Si_{0.65}Ge_{0.35}/Si$	100Å	N/A
1050	$Si/Si_{0.80}Ge_{0.20}/Si_{0.65}Ge_{0.35}/Si_{0.80}Ge_{0.20}/Si$	100Å	100Å

Table 4.1: Sample structures used in the band alignment study.

will be in the $Si_{1-x}Ge_x$ in both cases (Figure 4.5 (a)). If the alignment is type-II, a different PL energy will be observed in the STW structure than in the SW structure, because in the STW the PL will result from electrons in the $Si_{1-y}Ge_y$ cladding layer rather than the silicon layer as in the SW (Figure 4.5 (b)). The electrons in the Si layers can not recombine with the holes in the central $Si_{1-x}Ge_x$ well because they are spatially separated by the $Si_{1-y}Ge_y$ cladding layers. Assuming a barrier height of 5 meV and a transverse electron effective mass of $0.19m_e$, the penetration depth of the wave function ($|\phi|^2$) is only 30Å, which is well below the cladding layer thicknesses ($\geq$ 100Å). In the above analysis, a flat band condition in the well structure is always assumed. It can be easily proved that possible band bending due to charged carriers is negligible because of extremely small width of the wells. Assuming a net carrier concentration of $10^{16}/cm^3$ in a 100Åwide well, the relative band bending from the center to the edge of the well is only 0.2meV.

Two pairs of strained SiGe samples were grown using the technique of Rapid Thermal Chemical Vapor Deposition. One of each pair was a SW sample, such as $Si/Si_{0.65}Ge_{0.35}/Si$. The second of each group was a STW sample with the same central well Ge fraction, such as $Si/Si_{0.80}Ge_{0.20}/Si_{0.65}Ge_{0.35}/Si_{0.80}Ge_{0.20}/Si$. The structures of all four samples are listed in Table 4.1. The layers were thick enough to neglect complications from quantum confinement energy shift effects.

4.3 Photoluminescence Results and Discussion

The 4K photoluminescence spectra were taken using green light excitation from an argon-ion laser at a nominal power density of approximately $1W/cm^2$ with samples immersed in a liquid helium bath at Simon Fraser University in collaboration with M.L.W. Thewalt and L.C. Lenchyshyn. Well-resolved band-edge exciton PL was observed in all samples (Figure 4.6). The PL peaks labeled BE_{NP} are due to non-phonon recombination of shallow bound-excitons, and those labeled BE_{TO} are the transverse optical phonon replicas. The PL spectra from samples #1049 and #1050 have almost identical features with the non-phonon transition peak located at 906 meV and 904 meV, respectively, which is consistent with the same central well Ge fraction of 0.35 in both samples. At lower energies in the spectra are the transverse optical (TO) phonons and transverse acoustic (TA) phonon replicas of band edge exciton luminescence. The amount of displacement of the phonon replicas from the NP peak corresponds to the relevant phonon energy. Emission from sample #1006 and #1007 occurs at higher energies because of the lower Ge concentration in the central wells (x=0.20 in both samples). The no-phonon peak in the spectrum of #1006 occurs at 997 meV, while that of #1007 occurs at 994 meV. They are essentially equal (within the wafer-to-wafer variation of 5meV). The PL band labeled LE_{NP} about 15meV below the no-phonon peak in both samples is due to no-phonon recombination of the localized excitons due to alloy fluctuation [34] seen in some of our samples. The fact that in both sets of samples, the no-phonon bound exciton PL energies of the single well and the stepped well with an intermediate cladding layer were the same clearly suggests a type-I alignment (within 5meV) for Ge fraction up to 0.35.

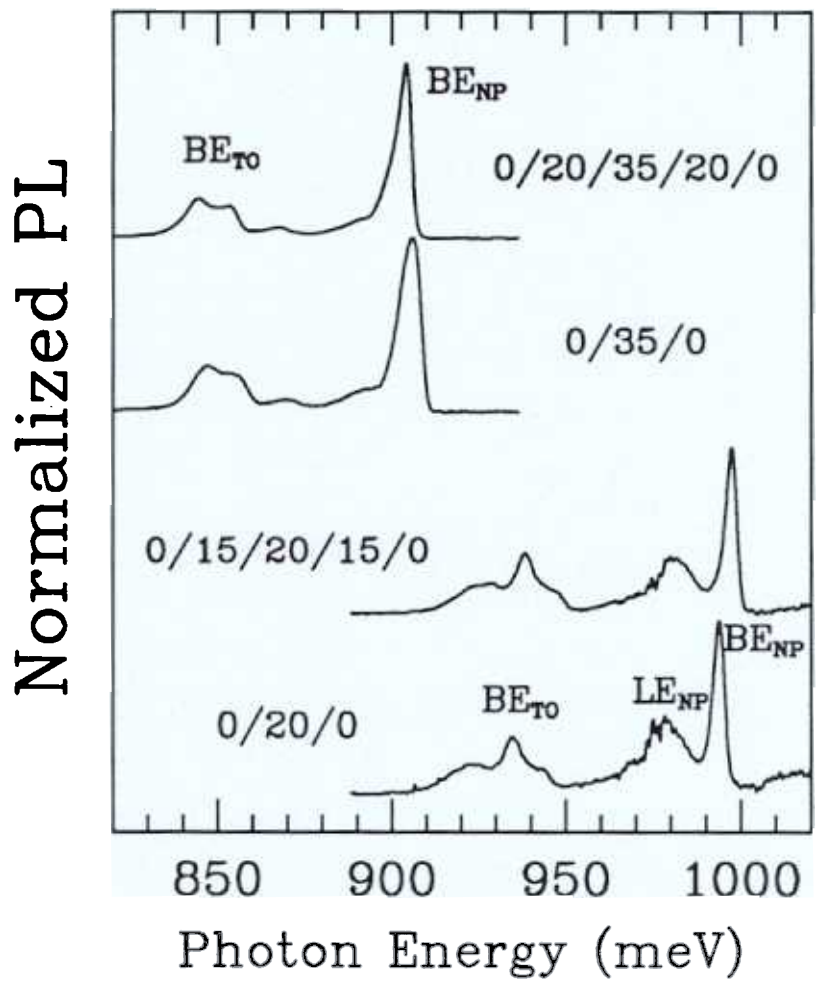

Figure 4.6: Photoluminescence spectra obtained at 4K from sample #1006, #1007, #1049, and #1050.

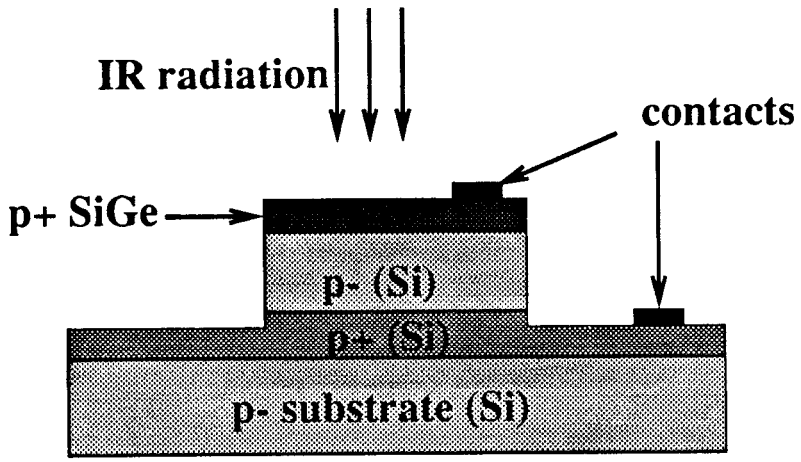

Figure 4.7: $Si_{1-x}Ge_x$/Si heterojunction internal emission

4.4 Measurement of ΔE_v by internal photoemission

Having shown that the photoluminescence from $Si/Si_{1-x}Ge_x/Si$ structures is due to recombination of electrons and holes which are both in the $Si_{1-x}Ge_x$ layer, the bandgap of the strained $Si_{1-x}Ge_x$ alloy can be obtained from the position of the no-phonon band-edge exciton recombination luminescence peak. The complete band alignment of strained $Si_{1-x}Ge_x/Si$ was then determined by combining this information with the valence band offset ΔE_V measured using heterojunction internal emission [35]. The measurement of ΔE_v by internal photoemission is discussed next.

When a p-type doped SiGe film is grown on top of a p-type silicon substrate, a rectifying junction will be formed at low temperatures due to the large valence band offset. When infrared radiation is incident on such a junction, holes in the SiGe layer can be excited by absorption of photons, and subsequently injected into the Si layer contributing a photocurrent (Figure 4.7). For infrared light with a photon energy below the valence band offset in the structure, no photocurrent will be observed because the excited holes will not have enough energy to overcome the potential barrier at the

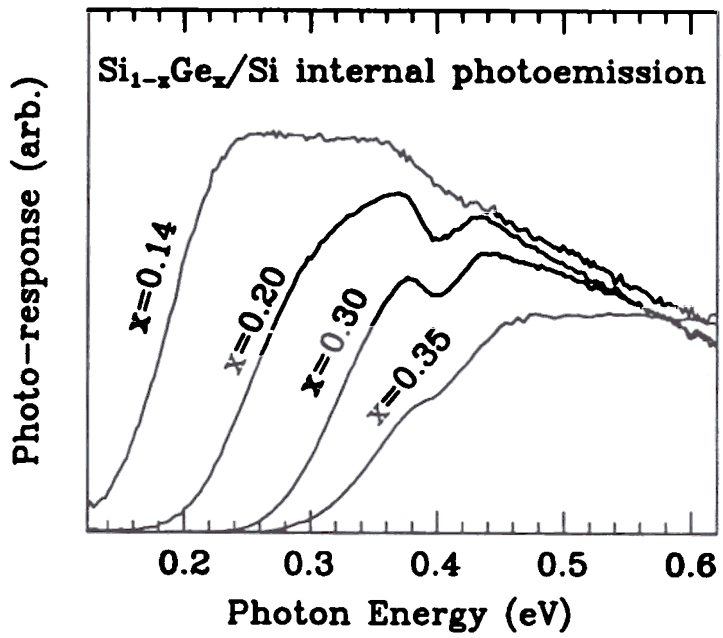

Figure 4.8: Infrared photoresponse vs. photon energy for several $Si_{1-x}Ge_x/Si$ heterojunctions. (Dips in some of the spectra at 0.4eV are due to absorption of the beam splitter in the FTIR spectrometer used in this experiment.)

$Si_{1-x}Ge_x$/Si interface. The energy which marks the onset of photocurrent (cut-off directly gives the corresponding valence band offset

A set of p-$Si_{1-x}Ge_x$/p-Si samples were grown for the internal photoemission measurements. To avoid heavy doping effects (such as bandgap narrowing and Fermi level moving well into the valence band), a thin layer of undoped $Si_{1-x}Ge_x$ spacer was inserted between the the heavily doped p-type $Si_{1-x}Ge_x$ and the p- silicon substrate. Diodes were fabricated on these samples by a simple mesa etch, and their infrared photoresponse due to internal photoemission of holes from $Si_{1-x}Ge_x$ layer into the silicon were obtained at 77K using a Fourier Transform Infrared(FT-IR) spectrometer. The long wavelength cut-off in the IR response directly gives the valence band

offset (ΔE_v) at $Si_{1-x}Ge_x$/Si interface (Figure 4.8). Note the uncertainty involved in determining the cutoff is mainly due to the lack of an established theory for the internal photo-emission response curve of a heterojunction, in contrast to that of a Schottky-barrier which can be modeled quite well by a modified Fowler theory.

Finally, combining the strained band gap data from band-edge photoluminescence and the valence band offset from heterojunction photoemission, the complete band line-up for the strained $Si_{1-x}Ge_x$/Si heterojunction was determined (Figure 4.9). Due to the uncertainties in both the valence band offset and band gap, it was not possible to determine the conduction band offset to a higher accuracy. Nevertheless, the results agree well with the calculation of van de Walle as shown by the solid lines in Figure 4.9, and they are also consistent with the type-I band alignment established by the comparative photoluminescence study of Si/$Si_{1-x}Ge_x$/Si single wells and Si/$Si_{1-y}Ge_y$/$Si_{1-x}Ge_x$/$Si_{1-y}Ge_y$/Si stepped wells discussed earlier.

4.5 Conclusion

By a comparative study of photoluminescence from Si/$Si_{1-x}Ge_x$/Si single wells and Si/$Si_{1-y}Ge_y$/$Si_{1-x}Ge_x$/$Si_{1-y}Ge_y$/Si stepped wells, the sign of the conduction band offset of the strained $Si_{1-x}Ge_x$/Si (100) interface has been directly determined, establishing a type-I band alignment. A combination of photoluminescence and heterojunction internal photoemission techniques was used to completely determine the band line-up for strained $Si_{1-x}Ge_x$ on (100) silicon, and the experimental results agree well with the theoretical calculation of van de Walle.

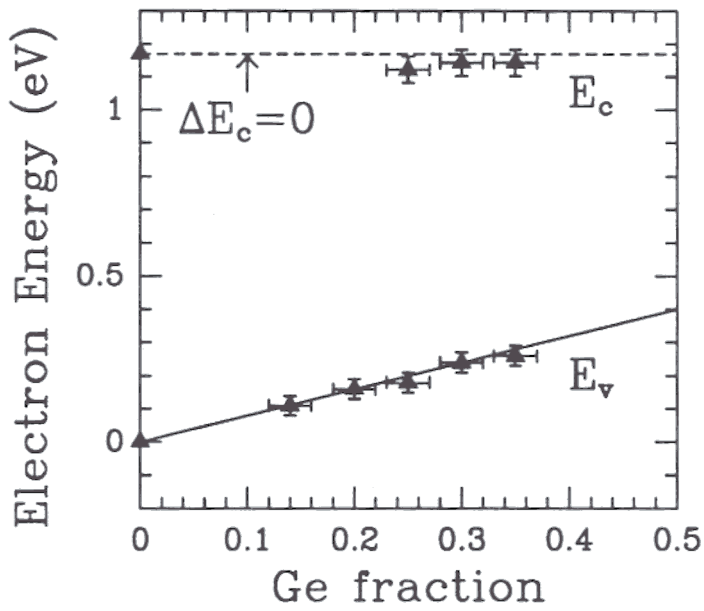

Figure 4.9: $Si_{1-x}Ge_x$/Si band alignment determined by a combination of photoluminescence and heterojunction internal photoemission.

Chapter 5

Photoluminescence Studies of Strained $Si_{1-x}Ge_x$ Quantum Wells

5.1 Introduction

One long-pursued goal of research in the field of strained silicon-germanium alloys is to fabricate active optoelectronic devices, such as infrared light-emitting devices on a silicon substrate. A detailed understanding of the physical processes underlying luminescence in $Si_{1-x}Ge_x$ alloys, especially at high carrier densities, is a prerequisite for any such attempt. Quantum wells play very important roles in light-emitting devices as can been seen in the development of III-V semiconductors lasers. As a result of carrier confinement provided by quantum wells, threshold current densities were dramatically reduced. In this chapter, we focus on two issues related to photoluminescence from strained $Si/Si_{1-x}Ge_x/Si$ quantum wells : photoluminescence (PL) line-shapes and quantum confinement shifts of PL energies.

5.2 Photoluminescence Line-shapes and an Electron-Hole-Plasma Model

At high carrier densities, degenerate electron-hole systems in both pure Si and pure Ge have been studied extensively and are well understood, but such systems have not been studied at all in $Si_{1-x}Ge_x$ strained layers. Such a study requires a growth technique capable of yielding material with well resolved excitonic features, which have only recently been observed [17, 18]. In this section, the observation of luminescence from electron-hole plasmas (EHP's) confined in $Si/Si_{1-x}Ge_x/Si$ quantum wells at 77K is reviewed.

5.2.1 Sample Structures and PL Spectra

The samples consisted of a nominally undoped single strained epitaxial $Si_{1-x}Ge_x$ quantum well between undoped epitaxial silicon layers. The samples were grown by a combination of Rapid Thermal Processing and Chemical Vapor Deposition [13] on (100) silicon substrates. Sample #728 has an atomic germanium fraction of $x = 0.20 \pm 0.02$ and a well width of 33 ± 3Å, determined by a combination of high resolution cross section transmission electron microscopy (HRTEM) and Rutherford back-scattering spectroscopy (RBS). The HRTEM and RBS measurements were done in collaboration with P.Fejes and R.B. Gregory of Motorola. Sample #729, grown under identical conditions, also has $x = 0.20$, confirmed by X-ray diffraction, and an expected $Si_{0.8}Ge_{0.2}$ width of 500Å. Based on previous experiments, the misfit dislocation density is expected to be much less than $10^2 cm^{-1}$. The photoluminescence (PL) spectra were taken using excitation from an argon-ion laser. 4K and 77K spectra were taken with samples immersed in liquid helium and liquid nitrogen baths, respectively. The spectra were measured in collaboration with M.L.W. Thewalt and L.C. Lenchyshyn of

Simon Fraser University.

At low temperature, the PL spectra (Figure 5.1) are dominated by luminescence due to shallow bound excitons, similar to what has been reported in Ref.[18]. The $Si_{1-x}Ge_x$ contribution to the spectra has a no-phonon (NP) transition as the highest energy component, and four phonon-assisted replicas at lower energies, which are attributed to the transverse acoustical (TA) phonon replica and to three distinct transverse optical (TO) replicas due to Ge-Ge, Ge-Si, Si-Si (Fig.5.1a). The spectrum of the 500Å sample (Fig.5.1b) appears similar to that of the 33Å sample, although at lower energies due to the absence of quantum confinement effects and with a somewhat wider linewidth (full-width half-maximum=10meV vs. 4meV for sample #728). relative intensities of the four phonon replicas, which will be used in fitting the high temperature spectra, are obtained from these low temperature spectra. The relative intensities of the Si-Si, Si-Ge and Ge-Ge TO phonon replicas agree very well with the statistical bond-counting model of Weber and Alonso [16].

At 77K, the PL spectrum shows two very broad peaks which are strongly dependent on the excitation power (Figure 5.2). In the 33Å-well sample, the lower edges of the luminescence lines hardly change while the high energy tails move upwards with increasing excitation power density. Because the sample was immersed in liquid nitrogen, it is thought that the high energy tail is not due to local heating. This was confirmed by fitting the luminescence of the TO replicas from the silicon substrate to a classical free exciton line shape [36], which gives sample temperatures differing from the bath temperature by 3 degrees in the worst case. (Because of the low carrier densities in the silicon layers, the free exciton model is valid.)

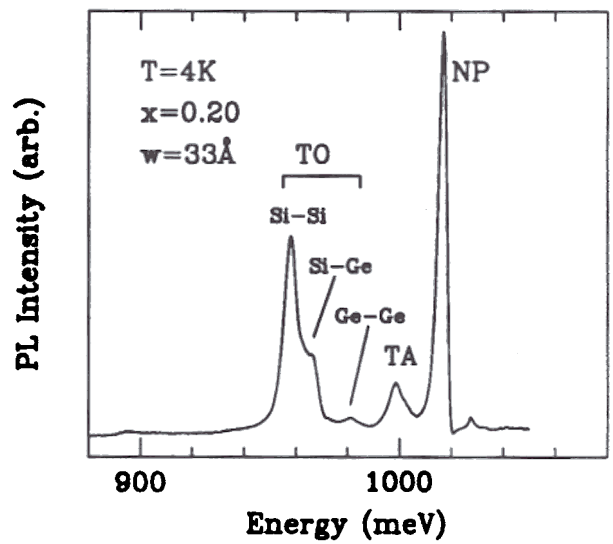

(a)

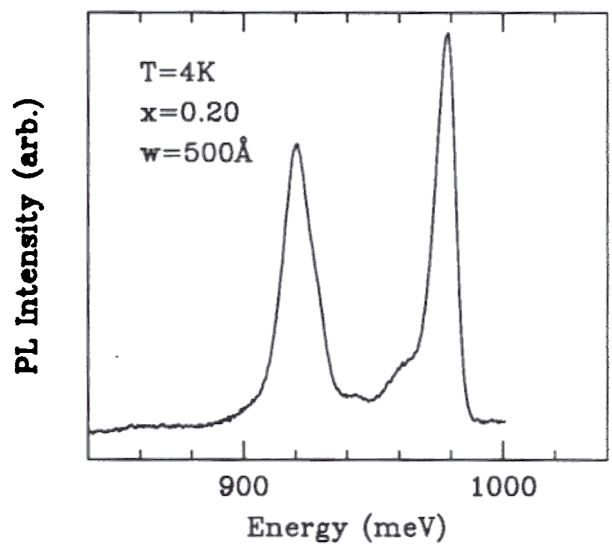

(a)

Figure 5.1: Low temperature PL spectra of (a) sample #728 (w = 33Å) and (b) sample #729 (w = 500Å).

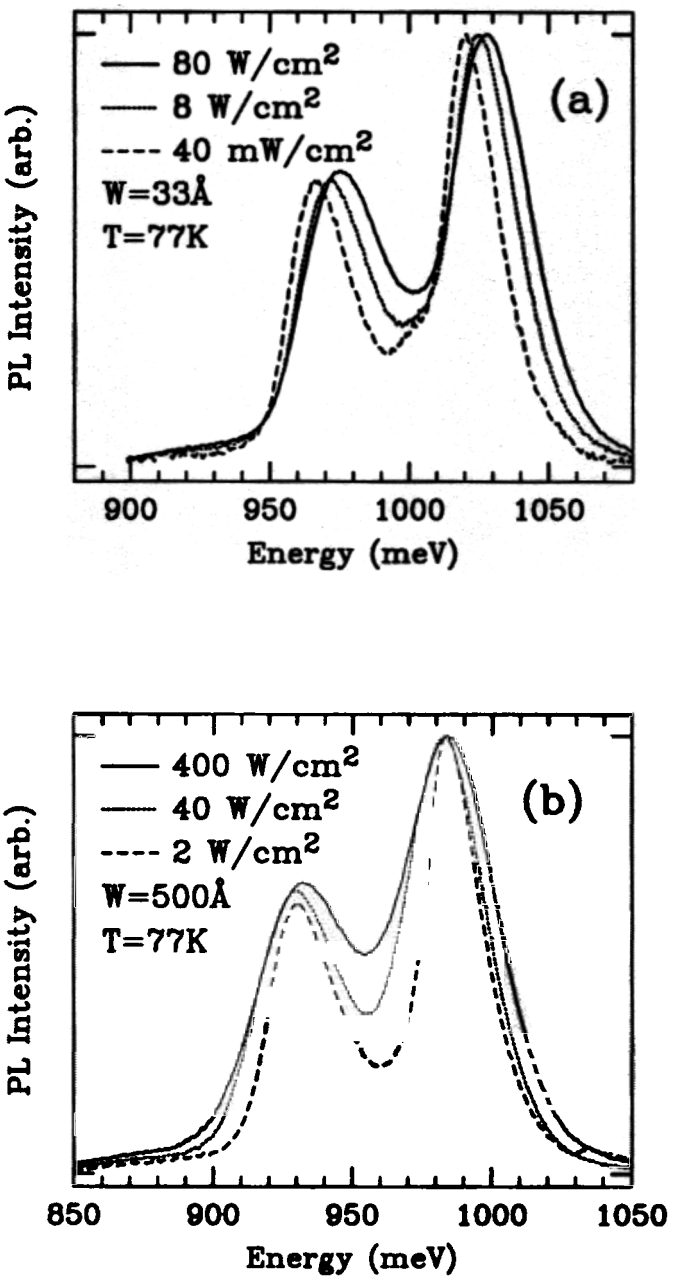

Figure 5.2: Excitation dependent PL spectra of (a) sample #728 and (b) sample #729.

5.2.2 The Electron-Hole-Plasma Model

The power dependence of the line shape of the $Si_{1-x}Ge_x$ emission precludes the possibilities of its origin in free excitons or in an electron-hole liquid (EHL) [37]. We identify this signal as luminescence from an electron-hole plasma confined in a $Si_{0.8}Ge_{0.2}$ quantum well. From other experiments in our lab, we have found that at 77K carriers generated in the silicon can travel long distances ($>> 0.1\mu$m) to be trapped in the $Si_{1-x}Ge_x$ quantum well [38]. The resulting carrier density in the well will then be much higher than that in the Si. The quasi-Fermi levels in the $Si_{1-x}Ge_x$ then move into the conduction and valence bands, resulting in the broadened line shape. To confirm this assignment, we fit the no-phonon line shape to the following expression for luminescence from EHP's [39]:

$$I(h\upsilon) = I_0 \int_0^{h\upsilon - E_{BB}} dE\ D_e(E) D_h(h\upsilon - E_{BB} - E) f(E, F_e, T) f(h\upsilon - E_{BB} - E, F_h, T) \quad (5$$

where D_e and D_h are the densities of states of electrons and holes, F_e and F_h are the electron and hole quasi-Fermi energies, $h\upsilon$ is the energy of the photon emitted, and E_{BB} is the renormalized bandgap due to the high carrier density for the EHP. The f's are the Fermi functions for electrons and holes. The electron Fermi energy F_e and hole Fermi energy F_h are related through charge neutrality. The line shape given by the above expression does not directly depend on the values of the density-of-states effective masses of electrons and holes. Rather, it depends only on the dimensionality of the carrier distribution and quasi-Fermi levels

As shown in Chapter 4, for strained $Si_{0.80}Ge_{0.20}$ on (100) silicon, the conduction band offset is very small, while the offset in the valence band is 160-180 meV. From a subband calculation which will be discussed in detail later in this chapter, for sample #728 which has a well width of 33Å, the lowest hole subband (HH_0) is separated from the nearest lying subband by about 35meV (Fig. 5.9) Therefore, the distribution

of holes in this narrow well was expected to be two-dimensional (constant $D_h(E)$). Sample #729 which has a well width of 500Å, however, was expected to have a 3-D hole distribution ($D_h(E) \propto \sqrt{(E)}$).

Another issue which needs to be addressed before attempting to fit the whole spectrum is the extensive overlap among the NP PL line and its phonon replicas at 77K. This is overcome by noting that, assuming constant phonon energies and matrix elements, these indirect transitions all have the same line shape no matter whether they are alloy-scattering-assisted as for the NP line or phonon-assisted as for the phonon replicas. To obtain the final spectrum, which is a simple summation of the no-phonon line and all the phonon replicas, one then needs to know the relative intensities of these various lines. For phonon replicas, the relative ratio is extracted from the 4K PL spectra, where they are well resolved. Due to the fact that at low temperature the PL is dominated by bound excitons, while at high temperature it is from an electron-hole plasma, the relative intensity of the NP line with respect to the phonon-assisted replicas is left as a adjustable parameter, which should only depend on the composition of the film. It should be pointed out that in doing so we have neglected higher-order processes such as two-phonon processes. There are in total three adjustable parameters for fitting: the relative weight of the NP line r_{NP}, the renormalized band gap for the EHP E_{BB}, and the sum of electron and hole Fermi energies $F = F_e + E_h$. While r_{NP} determines the relative height of the two peaks in the high temperature spectra, E_{BB} moves the spectrum along the energy axis, and Fermi energy F determines the line shape. The ratio of the Fermi energies F_e/F_h has little effect on the line shape.

With fixed r_{NP} and E_{BB}, varying F alone gives excellent fitting to all three spectra of sample #728 (33Å), as shown in Figure 5.3(a). The relative strength of the various TO peaks was not a function of pump power, and the fitting was done with a fixed relative TO intensity as described above. With increasing excitation, the line shape

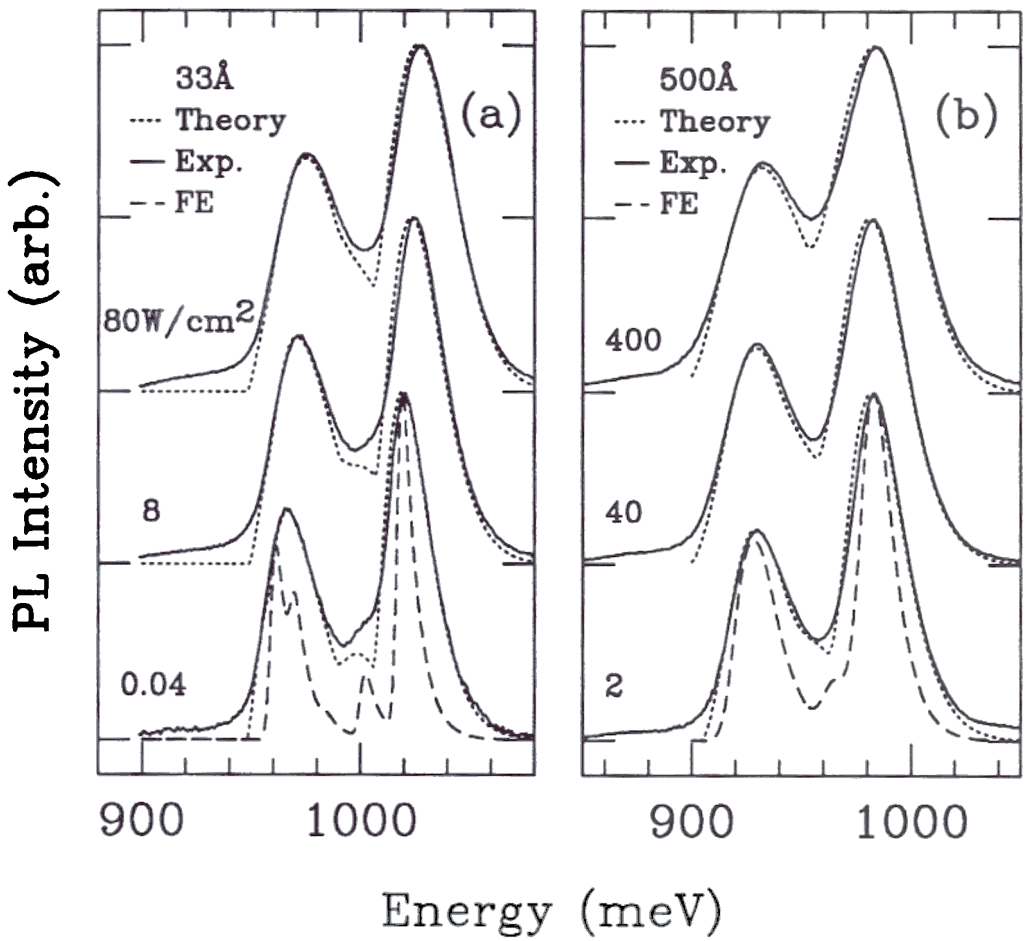

Figure 5.3: Theoretical fitting of the PL line-shapes using the EHP model

remains well behaved with the high energy tails shifting upwards, suggesting that no phase separation occurs between an electron-hole plasma and free excitons [39, 40]. In contrast to sample #728, which has a well thickness of 33 Å, sample #729 with a 500 Å well shows a quite different dependence of the line-shape on the excitation level (Figure 5.2(b)). As the excitation level increases, a pronounced change is found on the low energy side of the lines, and it was necessary to vary E_{BB} (renormalized bandgap) to obtain the fits of the model shown in Figure 5.3(b). The renormalized bandgap energies E_{BB} of both samples obtained from best fits are plotted versus excitation power density in Figure 5.4. While sample #728 (33Å well) shows less than 2meV change in E_{BB} over a range of more than 4 decades of excitation level, a reduction of 15 meV is evident for sample #729 (500Å well). This difference in bandgap renormalization suggests that there is a substantial difference in screening effects between 2-D and 3-D systems.

In our fitting of the spectra, we have entirely ignored free excitons, which usually dominate silicon PL at 77K at low power densities. This is now examined on both theoretical and empirical grounds. Theoretically, at low carrier densities electrons and holes form excitons, while at high carrier densities, excitons will dissociate into electron-hole plasmas. The Mott criterion [41] for such a FE-EHP transition is given by $n_c = k_B T/16\pi E_x a_x^3$ [39], where n_c is the critical carrier density above which an EHP is favored, E_x is the exciton Rydberg energy, and a_x is the exciton Bohr radius. Assuming Si-like effective masses, the critical density is $8.8\times10^{16}cm^{-3}$ at 77K. Using a simple model of densities of states for strained $Si_{0.8}Ge_{0.2}$, from our fitting we estimate carrier densities for the points of Fig. 5.4 from $\sim 2 \times 10^{17}cm^{-3}$ to $1 \times 10^{18}cm^{-3}$ in both sample #728 and sample #729. (The sublinear dependence of carrier density in the $Si_{0.8}Ge_{0.2}$ quantum well on pump power may be due to a reduction of the carrier collection efficiency into the quantum well because of band bending induced by charged carriers or due to increased non-radiative Auger recombination at high

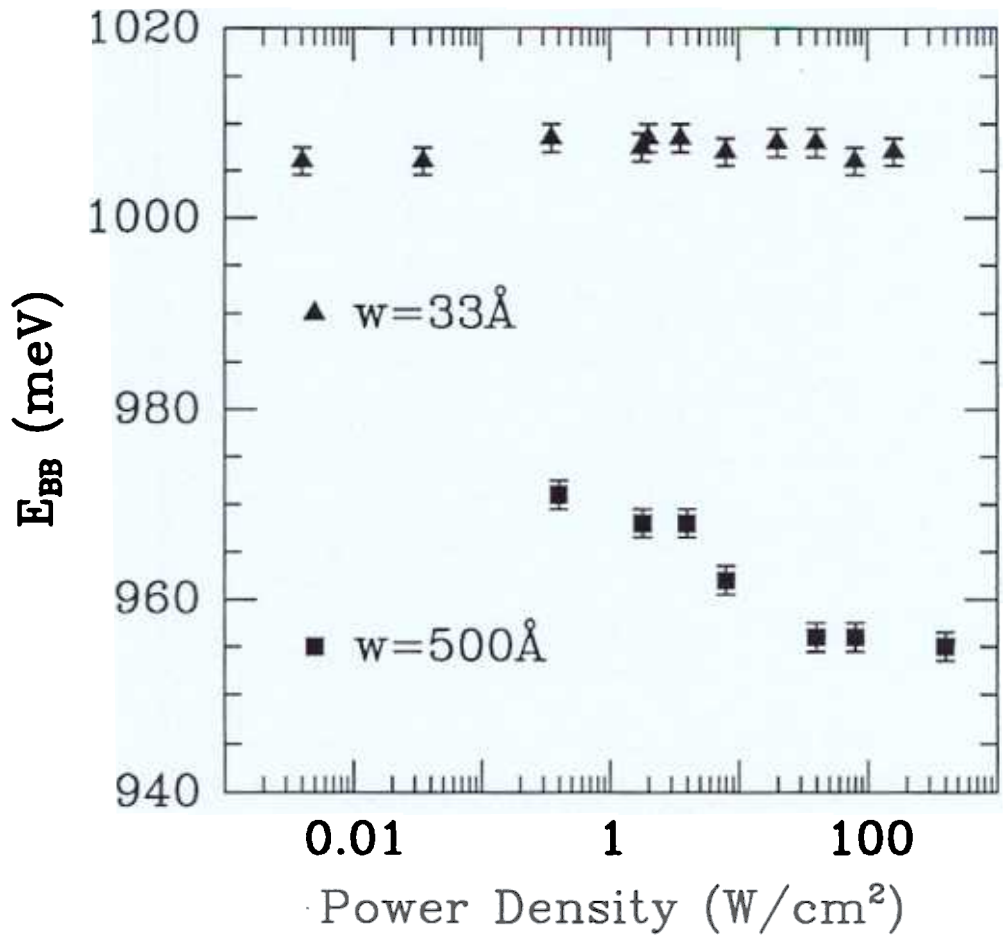

Figure 5.4: PL band-gap obtained from the best fit by EHP model versus excitation power density for both sample #728 and #729.

carrier densities.) These estimated carrier densities are well above the critical density for plasma formation at high power, but close to the transition criterion at low powers. Therefore we attempted to fit the spectra of sample #728 and #729 with with 2-D and 3-D free exciton models, respectively. As can be seen (fig. 5.3(a), (b)), a very poor fit was obtained. This leads us to believe that an electron-hole plasma is responsible for the luminescence at all power densities measured, except for possibly the 500Å sample at the lowest power density($0.4W/cm^2$), which has a line width close to that of a FE line-shape. At 60K, pure free exciton PL with a Boltzmann line-shape [18] has been seen in $Si/Si_{0.8}Ge_{0.2}$ superlattices (not isolated quantum wells) grown in the same reactor as sample #728 and #729. Although these superlattices were wider ($\sim$ 2500Å) than the quantum wells studied here and hence possibly had lower carrier densities, the reason for the different nature of the PL is not known.

5.2.3 Conclusion

We have observed photoluminescence from electron-hole plasmas confined in strained $Si_{1-x}Ge_x$ single quantum wells. At 77K, the PL spectrum shows significant line broadening as the excitation level is raised due to higher carrier concentrations in the quantum well. The PL spectra can be well fitted by a simple convolution of occupied electron and hole densities of states, with contributions from the NP line and the various phonon replicas included. While 2-D EHP's show little evidence of bandgap reduction, shift of the EHP renormalized band gap up to 15 meV has been observed for wide quantum wells.

5.3 Quantum confinement effects

In this section, a detailed study of the quantum confinement shifts of the band-edge photoluminescence energies in Si/strained $Si_{1-x}Ge_x$/Si single quantum wells (SQW)

is reviewed. A quantum confinement energy of up to 45 meV has been observed for quantum wells as small as 33 Å in width. The experimental results are in good agreement with a calculation of the hole confinement energies. The hole energy levels in the quantum wells were obtained by numerically solving effective-mass equations with proper matching of boundary conditions at interfaces using a 6×6 Luttinger-Kohn Hamiltonian. Both strain and spin-orbit interactions were included in the calculation.

5.3.1 Sample Structures

The structures used in the experiment are $Si/Si_{0.8}Ge_{0.2}$ quantum wells grown by Rapid Thermal Chemical Vapor Deposition [13] on 100 mm (100) silicon substrates. The silicon layers were grown at 700°C from dichlorosilane, and the silicon germanium layers at 625°C. Further growth details can be found in Ref. [13]. The $Si_{0.8}Ge_{0.2}$ layers were fully strained with a misfit dislocation spacing of greater than $100\mu m$ (determined by plane-view TEM on samples with similar structures). The thickness of the wells ranged from 33 to 83 Å. The Quantum well thickness was confirmed on several samples (33, 45, and 67 Å) by direct inspection by cross section transmission electron microscopy (TEM, done by P.Fejes of Motorola), and also independently by Rutherford Backscattering Spectroscopy (RBS, done by R.B. Gregory of Motorola). Assuming a $Si_{1-x}Ge_x$ composition of $x = 0.20 \pm 0.01$ (from X-ray diffraction measurement on thicker samples) and abrupt interfaces, the $Si_{1-x}Ge_x$ thickness can be easily calculated from the total 2-D Ge density measured by RBS. The two methods yielded the same thickness within 4%. From TEM and Auger electron spectroscopy profiling, the transition width at the interfaces was found to be 10 Å or less. On samples not measured as described above, the well widths were estimated by comparing the growth times to those of the above samples. The silicon cap layers were ~ 160Å thick for all samples.

5.3.2 Photoluminescence Results

The photoluminescence (PL) spectra were taken using green light excitation ($\sim$ 1W/cm^2) from an argon-ion laser. 4K and 77K spectra were taken with samples immersed in a liquid helium or liquid nitrogen bath, respectively (in collaboration with M.L.W. Thewalt and L.C. Lenchyshyn). The PL spectra of several of the samples with well widths ranging from 33 to 83 Å are shown in Figure 5.5 for 4K and 77K. By comparison to previous results in strained $Si_{1-x}Ge_x$ alloys [17, 18], the features in the spectra of Fig. 5.5 may immediately identified as band-edge exciton luminescence.

The highest-energy peaks in the 4K spectra represent no-phonon (NP) recombination of bound excitons primarily due to alloy randomness. At higher temperatures, such as 77K, the NP PL is from free excitons at low power densities [18] and from an electron-hole plasma (EHP) at high power densities [42]. Because no phonons are involved, the NP signal is an accurate measure of the bandgap except for exciton binding energies at 4K and renormalization effects due to the high carrier densities in the plasmas at 77K. This NP signal will be used in this paper to track the exciton energy in the quantum well. The lower-lying signals at both 4K and 77K are phonon replicas, of which the transverse optical is the most prominent [16, 18].

As the quantum well thickness is reduced, one notes a monotonic shift in the PL bandgap to larger values. This is expected because of the effect of quantum confinement on the energy levels in the well. To the best knowledge of the author, this is the first time this shift has been directly observed in the $Si/Si_{1-x}Ge_x$ system. The photoluminescence bandgaps extracted at 4K and 77K [42] are shown versus well width in Figure 5.6. The 77K PL bandgaps are consistently lower than the 4K PL bandgaps, presumably due to bandgap reduction at higher temperature and due to differences between the exciton binding energies and renormalization energies mentioned above. The relative shift of the bandgaps with well width is similar at both temperatures, however. The lines in Figure 5.6 are results from theoretical